



Simulating Cu electrodeposition in high aspect ratio features: Effect of control mode and uncompensated resistance in S-NDR systems



T.M. Braun*, D. Josell, T.P. Moffat

Materials Science and Engineering Division, National Institute of Standards and Technology, Gaithersburg, MD, USA

ARTICLE INFO

Article history:

Received 4 January 2021

Revised 3 February 2021

Accepted 6 February 2021

Available online 15 February 2021

Keywords:

Copper electrodeposition

Finite element method

Bifurcation

Instabilities

Electronics manufacturing

ABSTRACT

Void-free Cu electrodeposition in high aspect ratio features requires, at a minimum, an additive package containing micromolar halide and polyether that combine to form a co-adsorbed adlayer that inhibits metal deposition on the electrode interface. Successful feature filling relies on preferential growth proceeding from the most recessed surfaces where sustained breakdown of the polyether-halide suppressor layer occurs. Localization is the result of positive feedback between inhibitor breakdown and metal deposition subject to transport limitations of the suppressor precursor(s). This gives rise to a S-shaped negative differential resistance (S-NDR) that, convolved with uncompensated ohmic resistance, results in electrode bifurcation into active and passive zones. The interplay between the additive derived S-NDR behavior, uncompensated cell resistance, and potentiostatic regulation is explored in comparison to galvanostatic feature filling. Uncompensated resistance arises from the working electrode contact and electrolyte between the working and reference electrodes. For a $\text{CuSO}_4 - \text{H}_2\text{SO}_4$ electrolyte containing $80 \mu\text{mol/L Cl}^-$ and $40 \mu\text{mol/L}$ polyether, simulations of potentiostatic deposition with minimal uncompensated resistance reveal a narrow window between fully passive and voided feature filling; bottom-up filling terminates prematurely even under the most favorable conditions. In contrast, optimized galvanostatic operation enables void-free feature filling with termination dictated by coulometry. Increasing the uncompensated resistance along with application of accordingly more negative applied potentials produces filling dynamics that blend the positive attributes of galvanostatic and potentiostatic deposition to enable complete, void-free feature filling with spontaneous passivation near the feature opening. Importantly, these beneficial filling effects are also evident for trench arrays having variable widths or heights.

Published by Elsevier Ltd.

1. Introduction

Electrochemical deposition is widely used to fabricate microscale structures ranging from nanometer sized on-chip interconnects to larger scale wiring in printed circuit boards and related structures for microelectromechanical devices. Central to these applications is the need to fill high-aspect ratio recessed surface features. Typically, multicomponent additive packages are necessary for robust void-free filling of sub-micrometer trenches and vias. In the case of Cu electrodeposition, three components often used include a polyether-based suppressor, sulfonate-terminated thiol or disulfide accelerator, and some N-bearing leveler molecules, all of which have distinctive effects on the rate of metal deposition [1–12]. Superconformal feature filling results from competitive ad-

sorption between these species that, in the case of sub-micrometer features, includes the effect of area change on the coverage of the respective species [3–5]. For larger scale features, constraints on mass and charge transport become increasingly important to the filling process. Herein, the filling of larger features such as through silicon vias (TSV), whose depths approach or exceed the thickness of the adjacent hydrodynamic mass transport boundary layer, are examined. For these conditions, a more extreme form of preferential bottom-up feature filling is possible based on selective breakdown of a passivating layer that otherwise serves to block access of the metal cations to the electrode surface [13–24].

In the case of Ni [13,14], Co [15], and Au [16,17], only a single suppressing additive is required to induce this form of highly localized deposition while suppression of Cu deposition involves co-adsorption of a polyether and halide [25–42]. Polarization to sufficiently negative potentials disrupts the adlayer, permitting Cu^{2+} access to the electrode for electrodeposition [20–49]. In addition to applied potential, suppressor breakdown depends on the

* Corresponding author.

E-mail address: trevor.braun@nist.gov (T.M. Braun).

concentrations of its precursor components and hydrodynamics. Activation involves suppressor desorption and/or incorporation of some components into the growing deposit. It is also possible that the desorption process itself may be further stimulated by metal deposition. In either case, the positive feedback associated with potential-driven activation results in a sharp increase in deposition current and thereby significant hysteresis in cyclic voltammetry and galvanodynamic measurements. Operating at applied potentials within the hysteretic region leads to bifurcation of the electrode surface into active and passive reaction zones that give rise to Turing patterns on planar electrodes [18,50–56] and bottom-up filling of recessed electrode geometries such as through-holes and TSVs [18–24, 46–49]. The two phenomena are closely connected, resulting from differing time-scales between the ‘fast’ electronic response and ‘slow’ evolution of chemical gradients. The topography of the TSV substrate is coupled with local mass transport conditions that serve to guide the electrode bifurcation such that the planar field is passive due to a higher suppressor flux and active metal deposition occurs on the most recessed surfaces. An equally important contribution to the process is long range global coupling associated with the electrical response that is much faster than the development of suppressor and metal cation gradients driven by diffusion, electromigration, and sometimes convection. Indeed, it is the dynamic coupling between both effects that underlies the patterning associated with S-NDR systems [57–59]. Importantly, as pursued in detail herein, the strength of global coupling is a function of both the magnitude and spatial distribution of the uncompensated resistance in the system [57,58]. In a related fashion, the interaction between critical bistable systems and different regulation modes, controlled potential versus current, have been examined with particular attention to the important role of uncompensated resistance [59].

Uncompensated resistance includes ohmic losses associated with current flow in the electrolyte as well as external losses associated with the working electrode contacts that in combination cause the potential at the working electrode to deviate from the applied potential. The respective resistance values can be used as design parameters through various means. These include variation of the reference electrode position in 3-electrode systems, introduction of a porous, resistive baffle into the electrolyte between the reference and working electrode [60], and/or the insertion of an external resistor between the working electrode and the sensing point in the potentiostatic circuit [57–59]. In the case of a 2-electrode cell operating under constant applied potential, i.e., with the reference and counter electrodes shunted, an external in-line resistor can be introduced. However, in this instance additional knowledge of the counter electrode reaction characteristics is required for analysis of the working electrode overpotential. With the development of a suitable counter electrode it is interesting to contemplate the use of a 2-electrode cell run under constant applied potential as a useful variant to conventional galvanostatic operation, *vide infra*. Generalizing, if the shunted counter/reference electrode reaction is non-polarizable and the symmetry of the cell and workpiece are uniform, so that the lumped resistor approximations for the electrolyte can be used, then modeling of the 2- and 3-electrode configurations are analogous to one another. That said, in moving beyond 1-D models the location of the reference electrode, i.e., Haber-Luggin capillary, with respect to a multidimensional working electrode can be destabilizing to a uniform electrode state with the effect accentuated as the reference point is brought closer to the working electrode [56,57]. In the present 2-D simulations this concern is mitigated by sampling the reference potential at a plane within an idealized parallel plate cell where the potential is expected to be uniform based on the primary current distribution and the periodic nature and scale of the patterned workpiece.

Post-measurement correction for the uncompensated ohmic losses in conventional voltammetry reveals an inversion, or bistable S-shaped negative differential resistance (i.e., a decrease in driving force associated with an increase in reaction rate) that underlies the behavior of the suppressor based critical system. In the absence of ohmic losses, potentiostatic control within the S-NDR region is not viable as the system is unstable and jumps to either the active or passive branch. Rather, the presence of a significant uncompensated resistance enables operation within the hidden S-NDR region by providing a single valued applied potential for stable global potentiostatic operation while the bifurcation, accompanied by dynamic variations in overpotential and dissipative ohmic losses, evolves freely leading to pattern development. In contrast, galvanodynamic measurements enable the potential inversion associated with S-NDR critical systems to be revealed more directly by virtue of the single valued control points within the S-NDR region that enable a fixed deposition rate to be easily specified and maintained. The distinct path dependence of morphological evolution on planar electrodes for the respective control modes was recently highlighted in a microelectrode study of Cu deposition from the polyether – Cl⁻ suppressed CuSO₄ – H₂SO₄ system that serves to further motivate exploration of related effects during feature filling [52].

The important non-linear effects that arise from coupling resistive electrolyte losses with transport-constrained suppressor adsorption and its subsequent disruption by metal deposition were noted in earlier studies of extreme bottom-up filling of TSVs [18,43,44]. However the idea of engineering the uncompensated resistance to optimize feature filling has remained unexplored. Accordingly, the present work uses simulations of copper deposition in TSVs and trenches to compare feature filling dynamics during galvanostatic and potentiostatic deposition with an adjustable uncompensated resistance. The computations are built upon a suppressor co-adsorption S-NDR model that has been previously shown to capture feature filling dynamics and the relevant critical behavior [20]. The base case is potentiostatic deposition with a minimum uncompensated resistance, comparable to some recent experimental and computational work [20], that results in a narrow window for bottom-up filling subject to self-termination and incomplete filling of the TSVs and trenches examined. Recent theoretical and experimental studies have demonstrated that systematic stepping of the applied potential to more negative values (i.e., potentiodynamic control) can be used to adjust the termination point to achieve the desired level of filling [20,46–48]. More conventionally, optimized galvanostatic deposition enables stable filling of high-aspect ratio features for a limited range of applied currents with growth termination determined by coulometry. However, designing the system to have a larger uncompensated resistance, coupled with the associated increases in the applied potential, enables significant expansion of the operational window and void-free feature filling by the potentiostatic control mode. Furthermore, morphological evolution during filling under these conditions is nominally akin to that seen for galvanostatic deposition and, with optimization, the height of self-termination can be adjusted to match the feature opening. Another important attribute associated with optimized use of the uncompensated resistance is a significant improvement in the ability to fill both simple and complex trench arrays under a fixed applied potential. Interestingly, iterative filling of individual recessed features may occur within the array when applied potentials are at the more positive end of the hysteretic window [19]. For galvanostatic control this has an interesting analogy to the bifurcation reactions on microelectrode arrays where the individual microelectrodes not only sequentially switch from the passive to active state as the applied current density is increased but can also exhibit oscillatory behavior [61,62]

2. Computational methods

Finite element method (FEM) computations are used to simulate copper electrodeposition in 2D axisymmetric annular and cylindrical through-silicon vias and 2D trench arrays. The dimensions of the annular TSV (inner radius $R_i = 4 \mu\text{m}$, outer radius $R_o = 9.5 \mu\text{m}$, and height $H = 56 \mu\text{m}$) match those of prior experimental work [13–20,43,44]. Simple cylindrical TSV having radius $R_{cyl} = 5 \mu\text{m}$ and height H_{cyl} ranging from 50 to 200 μm , corresponding to aspect ratios from 5 to 20, were also examined. Trench arrays were simulated in a 4×1 configuration with dimensions of trench width $W_t = 10 \mu\text{m}$, trench height $H_t = 50 \mu\text{m}$, and pitch $P_t = 20 \mu\text{m}$ between trench edges. The 2D configuration assumes a trench length of 1 mm. More complex trench arrays having a 3×1 configuration with varying trench width from 10 to 30 μm and trench height from 50 to 100 μm were also examined. For all workpiece geometries, the reference electrode (RE) and counter electrode (CE) were combined in a common plane opposite the working electrode (WE) at a distance L , and the electric potential was fixed at zero. For the base case, L was taken to be 0.25 cm, thereby specifying the uncompensated resistance between the working and reference electrode. This gives a potential drop that was nominally equal to that observed in recent experimental work with annular TSV albeit for a less well-defined electrochemical cell configuration [19,20]. The hydrodynamic boundary layer thickness, δ , is set to 25 μm in all simulations and the concentration of each species (Cu^{2+} , Cl^- , and polymer) is set equal to that of the bulk solution (C_i^0) at these boundaries. The solution conductivity, κ , for the 1.0 mol/L CuSO_4 -0.5 mol/L H_2SO_4 equals 15.26 S/m [18]. Each simulation begins with a 2 min incubation period that emulates an experimental setup where patterned electrode fragments are pretreated with an ethanol wetting solution prior to insertion into the plating solution and subsequently idled for 2 min at a small overpotential before stepping to the much more negative applied potential. Computationally, this is approximated with an applied potential of -0.40 V (or current equal to 1% of the set value) for 2 min before stepping to the set value. Initial concentrations are $0.01C_i^0$ in the electrolyte domain contained within the hydrodynamic boundary layer to emulate electrolyte exchange with the ethanol filled features.

Variation in the uncompensated resistance between the reference and working electrodes is examined computationally using three different schemes: (a) alteration of the distance between the reference and working electrodes, (b) insertion of a baffle into the electrolyte phase with fine scale porosity that effectively increases the resistance between the working and reference electrodes, and (c) insertion of an external resistor between the sensing point on the working electrode and the actual metal/electrolyte interface. All three approaches have been used by experimentalists for various ends. The first provides a simple method to evaluate the effect of the electrochemical cell time constant ($\tau \sim \text{resistance} \times \text{capacitance}$, RC). Baffles have been used in commercial electroplating cells to counter the terminal effect that otherwise leads to non-uniform deposition on resistive seed layers [60]. The introduction of the external resistor in series with a 2-electrode cell has been used to examine the effects of variation in the experimental control mode, from potentiostatic to galvanostatic, and its impact on pattern formation in bistable systems, a subject of central interest in the present work [58,59].

The focus of this study is the consequence of, not the pathway to, increasing the uncompensated resistance. Considering the uncompensated ohmic drop in the context of the electrolyte conductivity and the geometric configuration of the cell, with the working and counter electrodes positioned at opposite ends of a circular tube of radius R_c , allows the ohmic losses due to current flow in

the electrolyte to be defined by

$$\Omega_s = \frac{L}{\pi R_c^2 \kappa}. \quad (1)$$

For a given workpiece, area is taken to define the cross sections of the cell (i.e., πR_c^2) so that changes in Ω_s are accomplished by adjusting the distance from the RE/CE relative to the working electrode (WE), L , or through the solution conductivity, κ . A series of calculations were performed where Ω_s is increased by a factor of 6, 9, 11, 21, 41, 81, 161, or 401. This can be realized via Eq. (1) by an increase in L from 0.25 cm to 1.5, 2.25, 2.75, 5.25, 10.25, 20.25, 40.25, and 100.25 cm, respectively. Alternatively, the same effect can be obtained by holding L at 0.25 cm and increasing the effective κ by insertion of a porous and electrically insulating baffle whose net effect on ohmic losses is a composite of the respective material properties. In the present work the insertion of a baffle is approximated by giving a thin slice of the electrolyte (25 μm thick) adjacent to the RE/CE plane a lower conductivity (e.g., $500 \times$ to $20,000 \times$ lower) than that of the actual electrolyte conductivity, κ . This effectively increases the uncompensated resistance by $11 \times$ to $201 \times$ the default Ω_s based on the homogenous solution conductivity and $L = 0.25$ cm. Finally, the uncompensated resistance can similarly be manipulated by inputting an external resistor, that is some multiple of Ω_s , between the WE and RE contacts (or CE/RE plane in the current construct). Given the symmetry of the cell and workpiece, the first important conclusion is that despite differences in the location of the uncompensated resistance within the cell, simulations of equivalent total resistance produce identical results regardless of which method is implemented, provided that the baffle is located sufficiently far from the working electrode that it does not influence the development of chemical gradients. Adjusting the position of the RE/CE plane is the most computationally demanding as it requires additional meshing that leads to longer computational times. From an experimental standpoint, integrating uncompensated resistance as a *variable* control parameter into an existing 2- or 3-electrode system is most easily realized by the external resistor approach. As such, all simulations presented herein use an external resistor to adjust the overpotential to account for the potential drop associated with the deposition current flowing through the external series resistor in order to model the impact of a modified global cell resistance.

The concentration C_i (and flux N_i) of each species in the electrolyte domain is described by the Nernst-Planck equation, capturing both diffusion and electromigration, such that the evolution of concentration is given by

$$\frac{\partial C_i}{\partial t} = -\nabla \cdot \vec{N}_i = -\nabla \cdot (-z_i u_{m,i} F C_i \nabla \phi - D_i \nabla C_i) \quad (2)$$

given the species' charge z_i , diffusion coefficient D_i , Faraday's constant F , and mobility $u_{m,i}$ calculated by the Einstein relationship

$$u_{m,i} = \frac{D_i}{RT}. \quad (3)$$

The simulated electrolyte assumes full dissociation of CuSO_4 and NaCl , reasonable for the relevant concentrations of Cu^{2+} and Cl^- , while the speciation and gradients associated with hydronium, sulfate, bisulfate, and sodium were not evaluated. The poloxamine suppressor (subscript P) is assumed to be neutral in charge ($z_p = 0$). Diffusion coefficients listed in Table 1 for Cu^{2+} , Cl^- , and poloxamine tetronic (TET) are taken or estimated from literature sources [20,63–67].

Due to the high concentration of CuSO_4 and the H_2SO_4 supporting electrolyte, potential in the electrolyte (ϕ) is well approximated by the Laplace equation

$$\nabla^2 \phi = 0, \quad (4)$$

Table 1
Parameters for mm-TSV simulations.

Parameter	Name	Units	Value	Reference
<u>Annular TSV Cell Geometry</u>				
inner radius	R_i	μm	4	[20]
outer radius	R_o	μm	9.5	[20]
height	H_{ann}	μm	56	[20]
cell radius	$R_{c,ann}$	μm	26	[20]
cell resistance	Ω_s	Ω	76,600	-
<u>Cylindrical TSV Cell Geometry</u>				
radius	R_{cyl}	μm	5	-
height	H_{cyl}	μm	50 to 200	-
cell radius	$R_{c,cyl}$	μm	26	-
cell resistance	Ω_s	Ω	76,600	-
<u>Trench Array Cell Geometry</u>				
width	W_t	μm	10 to 30	-
height	H_t	μm	50 to 100	-
length	L_t	mm	1	-
spacing	P_t	μm	20	-
cell resistance	Ω_s	Ω	1363	-
<u>General Cell Geometry</u>				
boundary layer thickness	δ	mm	25	-
reference electrode position	L	cm	0.25	-
<u>Electrolyte Parameters</u>				
bulk concentration Cu^{2+}	C_{Cu}^o	mol/L	1	-
bulk concentration Cl^-	C_{Cl}^o	$\mu\text{mol/L}$	80	-
bulk concentration polyether (Poloxamine Tetronic 701)	C_p^o	$\mu\text{mol/L}$	40	-
diffusion coefficient Cu^{2+}	D_{Cu}	cm^2/s	5×10^{-6}	[63]
diffusion coefficient Cl^-	D_{Cl}	cm^2/s	9×10^{-6}	[20]
diffusion coefficient polyether (Poloxamine Tetronic 701)	D_p	cm^2/s	1×10^{-6}	[65–67]
electrolyte conductivity	κ	S/m	15.26	Measured
reversible Potential	E_{rev}	V	-0.38	Measured
<u>Adsorbate Parameters</u>				
saturation chloride coverage	Γ_{Cl}	mol/m^2	1.62×10^{-5}	[20]
saturation suppressor coverage	Γ_p	mol/m^2	9.2×10^{-8}	[69]
chloride adsorption kinetics	k_{Cl}^+	$\text{m}^3/(\text{mol}\cdot\text{s})$	20	[20]
chloride deactivation kinetics	k_{Cl}^-	1/m	1.5×10^7	[20]
suppressor adsorption kinetics	k_p^+	$\text{m}^3/(\text{mol}\cdot\text{s})$	2500	[20]
suppressor deactivation kinetics	k_p^-	1/m	1×10^7	[20]
initial chloride & polymer coverages	$\theta_{i,o}$		0	-
<u>Electrochemical Kinetics</u>				
unsuppressed Cu exchange current density	j_0^o	A/m ²	20	[20]
suppressed Cu exchange current density	j_1^o	A/m ²	0.13	[20]
unsuppressed charge transfer coefficient	α_0	-	0.5	[20]
suppressed charge transfer coefficient	α_1	-	0.5	[20]
Cu ionic charge	n	-	2	-
Cu molar volume	Ω	m^3/mol	7.1×10^{-6}	-
<u>Miscellaneous</u>				
applied potential (potentiostatic)	V_{app}	V	-0.46 to -2.18	-
applied current (galvanostatic)	i_{app}	μA	-0.016 to -400	-
uncompensated cell resistance	Ω_{cell}	Ω	$1\Omega_s$ to $401\Omega_s$	-
pretreatment time	t_{pre}	s	120	-
pretreatment potential (potentiodynamic case)	V_{pre}	V	-0.40	-
pretreatment current (galvanostatic case)	i_{pre}	mA/cm^2	$0.01i_{app}$	-
temperature	T	K	293	-

which neglects potential variation in solution arising from ionic gradients. The current density \vec{j} associated with the Cu^{2+} flux through the electrolyte is given by Ohm's law

$$\vec{j} = -\kappa \nabla \phi. \quad (5)$$

where κ is the solution conductivity. A zero flux symmetry condition is imposed on the side of the cell (at $r = R_c$ in axisymmetric simulations and $x = 0$ and $x = 12 W_t$ in 2D trench simulations) for gradients of solution potential

$$\frac{\partial \phi}{\partial r} = 0 \text{ or } \frac{\partial \phi}{\partial x} = 0 \quad (6)$$

and gradients of concentration

$$\frac{\partial C_i}{\partial r} = 0 \text{ or } \frac{\partial C_i}{\partial x} = 0. \quad (7)$$

Accumulation of adsorbates on the electrode follows Langmuir adsorption kinetics with deactivation of suppression related to

metal deposition involving a combination of desorption and/or incorporation into the growing deposit. Evolution of the fractional chloride coverage θ_{Cl} , defined as the surface concentration divided by the saturation coverage, is described by

$$\frac{\partial \theta_{\text{Cl}}}{\partial t} = k_{\text{Cl}}^+ C_{\text{Cl}} (1 - \theta_{\text{Cl}}) - k_{\text{Cl}}^- \theta_{\text{Cl}} \nu \quad (8)$$

where k_{Cl}^+ is the adsorption rate constant, C_{Cl} is the chloride concentration at the evolving metal/electrolyte interface, k_{Cl}^- is the deactivation rate constant and ν is the metal deposition rate. Evolution of the fractional poloxamine coverage, θ_p , is described by the analogous equation

$$\frac{\partial \theta_p}{\partial t} = k_p^+ C_p (\theta_{\text{Cl}} - \theta_p) - k_p^- \theta_p \nu \quad (9)$$

where the poloxamine is restricted to adsorption on top of the halide covered sites and thereby implicitly subject to the requirement that θ_p cannot exceed θ_{Cl} through adsorption. The fractional

chloride and poloxamine coverages are further limited to values between 0 and 1. Values for k_i^+ and k_i^- listed in Table 1 are estimated from model fits to the hysteretic voltammetry with the fitting procedure focused on capturing the critical onset potential for suppressor breakdown as a function of suppressor and halide concentration [20,44]. In previous efforts the critical breakdown potential was shown to be dominated by the higher rate of Cl^- adsorption and consumption relative to that of the polymer. Once a fully developed Cl^- -polyether adlayer exists, Cl^- consumption into the solid by the second term on the right side of Eq. (8) can make the adsorption term for the suppressor in Eq. (9) effectively function as a desorption term.

The metal deposition rate is assumed to be a function of the suppressor coverage θ_p (or, equivalently, coverage of the polyether-chloride bi-layer), metal ion concentration C_{Cu} , and overpotential η at the interface, thus

$$v(\theta_p, C_{\text{Cu}}, \eta) = \frac{\Omega}{nF} \frac{C_{\text{Cu}}}{C_{\text{Cu}}^0} [j_{\theta=0}(\eta)(1 - \theta_p) + j_{\theta=1}(\eta)\theta_p]. \quad (10)$$

The overpotential-dependent current densities on unsuppressed ($j_{\theta=0}$) and suppressed ($j_{\theta=1}$) surfaces for the two electron reduction of Cu^{2+} to its metallic form are thus translated into growth velocity, v , using Faraday's constant ($F = 96,485 \text{ C/mol}$), the ionic charge n , and the molar volume Ω of solid copper. This simple form captures suppression arising from the polyether coverage (as limited by chloride coverage). The current densities ($j_{\theta=0,1}$) are assumed to exhibit the conventional exponential dependence on overpotential η by

$$j_{\theta=0,1}(\eta) = j_{\theta=0,1}^0 \left(e^{\frac{(1-\alpha_{\theta=0,1})F}{RT}\eta} - e^{-\frac{\alpha_{\theta=0,1}F}{RT}\eta} \right). \quad (11)$$

The applied potential V_{app} is related to the overpotential at the working electrode through

$$V_{\text{app}} = \eta + \phi + E_{\text{rev}} \quad (12)$$

where the potential ϕ within the electrolyte is evaluated at the electrolyte/deposit interface to capture the dissipative losses (i.e., iR -drop) between the workpiece and the reference electrode associated with current flow through the electrolyte and external resistor layer. The overpotential driving electrodeposition is referenced to the reversible Nernst potential for the Cu^{2+}/Cu reaction. The values of $j_{\theta=1}^0$ and $\alpha_{\theta=1}$ for the fully suppressed surface are obtained by fitting the negative-going voltammetric scans up to the onset of suppression breakdown [20,52]. Although the kinetics of copper deposition on polymer-free surfaces are known to be a function of halide coverage, for simplicity, the present work uses a single set of $j_{\theta=0}^0$ and $\alpha_{\theta=0}$ values for deposition on the polymer-free surface, as in previous feature filling simulations.

The local current density at the electrode is equated to the Cu^{2+} flux from the electrolyte onto the electrode interface (outward surface normal \hat{n}) according to

$$\frac{1}{nF} \vec{j}_{\text{Cu}} \cdot \hat{n} = -(z_{\text{Cu}} u_{\text{m,Cu}} F C_{\text{Cu}} \nabla \phi + D_{\text{Cu}} \nabla C_{\text{Cu}}) \cdot \hat{n}. \quad (13)$$

Similarly, the normal fluxes of chloride and polyether from the electrolyte to the interface are equated to the rates of their adsorption yielding

$$-(z_{\text{Cl}} u_{\text{m,Cl}} F C_{\text{Cl}} \nabla \phi + D_{\text{Cl}} \nabla C_{\text{Cl}}) \cdot \hat{n} = \Gamma_{\text{Cl}} k_{\text{Cl}}^+ C_{\text{Cl}} (1 - \theta_{\text{Cl}}) \quad (14)$$

and

$$-(D_p \nabla C_p) \cdot \hat{n} = \Gamma_p k_p^+ C_p (\theta_{\text{Cl}} - \theta_p) \quad (15)$$

with saturation coverages Γ_i estimated from literature [20,68,69]. As stated previously, the $(\theta_{\text{Cl}} - \theta_p)$ term captures the requirement that suppressor adsorption only occurs at chloride covered surface sites.

The full system of equations is solved numerically in 2D and 2D-axisymmetric geometries using a finite element method employed in the COMSOL Multiphysics version 5.5 software package with the default solver, implementing the following modules: Tertiary current distribution, primary current distribution, separate coefficient form boundary partial differential equations for both chloride and suppressor, and deformed geometry. The 2D triangular mesh elements are more highly refined along the electrode interface, their dimensions initially equal to 20% of the feature radius or width on each side. The mesh scales up to a maximum of $2.5 \mu\text{m}$ within the boundary layer and $26 \mu\text{m}$ outside of the boundary layer. The mesh in the thin resistive layer is also refined, having a maximum size of $5.2 \mu\text{m}$. Automatic remeshing is enabled, prompting re-mesh when the maximum mesh distortion parameter exceeded 1.56. A moving boundary smoothing parameter of 2, geometry shape order of 1, and Laplace mesh smoothing type are used in the deformed geometry module (see COMSOL documentation for detailed explanation on how these parameters impact moving boundary convergence). The system of equations was solved so that the overall charge imbalance (the fractional difference between the total integrated currents at the counter and working electrodes) was less than 0.02%. The numerical evaluation error, thus, is acceptably small for the present purposes. To give a sense of the computational expense, the smaller geometry simulations having 1800 domain and 400 boundary mesh elements take on the order of 5 min to compute. Larger simulations having 5000 domain and 800 boundary mesh elements take on the order of 30 min to compute. All simulations used a Dell Precision 3630 desktop computer with an Intel Xeon E-2186 G CPU @ 3.80 GHz and 64 GB RAM using a Windows 10 Enterprise 64-bit operating system.

3. Results and discussion

Experimental copper deposition in through-silicon vias has been previously detailed in electrolytes having a single suppressing polyether additive for a range of chloride concentrations (2 to $1000 \mu\text{mol/L}$) and combinations of CuSO_4 and H_2SO_4 concentrations [18–20,47,48]. In low chloride solutions ($\leq 80 \mu\text{mol/L}$), copper deposition initially occurs on the bottom of the via as well as the neighboring sidewalls up to a position marking a transition between active and passive plating regions. This transition point shifts upward in the via with lower chloride concentrations or more negative potentials [20]. At fixed potential, deposition is eventually quenched at a position within the via determined by the balance between transport constrained adsorption of the suppressing additives and its disruption by the metal deposition reaction. Accordingly, for these low chloride electrolytes it is necessary to step or ramp the potential to more negative values in order to fully fill features [20,46–48]. This approach requires tuning the applied potential waveform to optimize filling. For stepped potentials, the discontinuous nature of the increase in available free energy might be expected to impact, or mark, the deposit microstructure. Alternatively, galvanostatic deposition provides both operational simplicity and cost advantages in process control, congruent with its use in industrial electroplating practice. Deposition is sustained as long as the current is applied and with proper optimization void free filling is possible. If the applied current is too high void formation will occur, while too low a value will result in uneven activation of deposition across the workpiece. Even with an appropriate value of applied current substantial under- or over-fill will occur if the deposition time is not tuned appropriately for each substrate pattern. In contrast, potential-controlled deposition offers an alternative path to feature filling based on spontaneous self-passivation that calculations indicate to be less sensitive to variations in pattern density on the work piece.

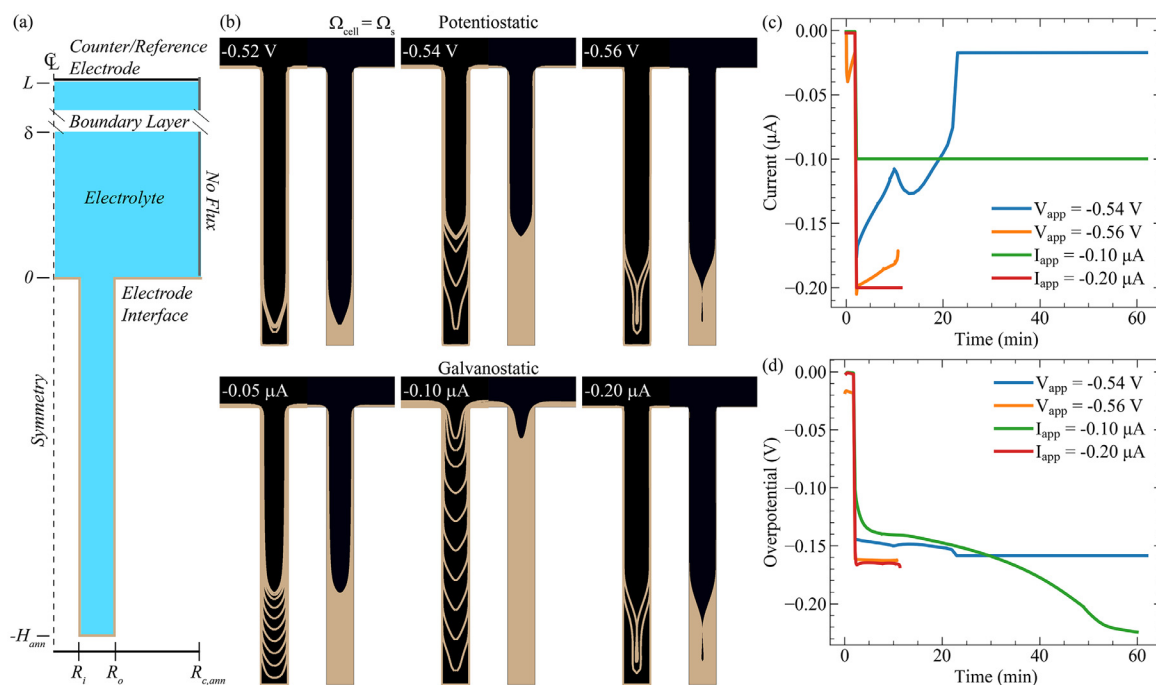


Fig. 1. (a) Schematic of the axisymmetric geometry used in the S-NDR model to simulate deposition in the annular TSV with dimensions of $R_i = 4 \mu\text{m}$, $R_o = 9.5 \mu\text{m}$, and $H_{\text{ann}} = 56 \mu\text{m}$. Relevant domains and boundaries are indicated. (b) Simulated growth contours in 6 min intervals (left-hand via) and final deposit positions (right-hand via) for potentiostatic (top) and galvanostatic (bottom) copper electrodeposition after 1 h at the indicated operating conditions. (c) Current and (d) overpotential, η , transients for the indicated simulations presented in (b).

3.1. Deposition in annular TSV

Fig. 1 shows simulated final growth profiles and interface contours (in 6 min intervals) for potentiostatic and galvanostatic deposition in 1 mol/L CuSO_4 , 0.5 mol/L H_2SO_4 , 40 $\mu\text{mol/L}$ TET, and 80 $\mu\text{mol/L}$ Cl^- for the annular TSV configuration shown schematically in Fig. 1a. The cell and workpiece geometry have been previously detailed both experimentally and computationally for potential-controlled deposition with $L = 0.25 \text{ cm}$ [20]. As discussed above, the simulations of potentiostatic deposition do not predict complete filling even under conditions yielding deposition localized to the via bottom. Rather, passivation occurs less than halfway up the via after ≈ 20 min at -0.54 V . Deposition at -0.52 V passivates even earlier, after ≈ 6 min, filling just the lowermost 4 μm of the 56 μm tall feature (i.e., $z = -52 \mu\text{m}$). At a more reducing potential of -0.56 V deposition is predicted to yield void formation after 8.5 min. Galvanostatic deposition, conversely, results in a nearly filled feature at $-0.10 \mu\text{A}$ after 1 h of deposition with the applied current appropriately tuned to the relevant electrochemically active surface area in the present case. A factor of 2 decrease in the applied current results in only 1/3 of the feature being filled after 1 h before localized bottom-up deposition is lost and the applied current redistributes across the entire surface, with a corresponding $7 \times$ decrease from the peak current density during bottom-up fill. At the other limit, a doubling of the applied current leads to void formation after 9 min.

Current and overpotential transients in Fig. 1c and Fig. 1d, respectively, provide insight into the growth dynamics under potentiostatic deposition at -0.54 and -0.56 V for the base case with an uncompensated resistance of $1\Omega_s$ and, for the same geometry, galvanostatic deposition at -0.10 and $-0.20 \mu\text{A}$. Determining the appropriate area for current density scaling is a challenge for bifurcating systems given the temporally varying active electrode area. That said, an applied current of $-0.10 \mu\text{A}$ corresponds to -4.7 mA/cm^2 when scaling by projected electrode area,

-42.9 mA/cm^2 when using only the via bottom, and -1.45 mA/cm^2 when using the entire electrode interface, signifying the available current density range depending on what portion of the surface is electrochemically active. Each simulation begins with a 2 min incubation period to emulate experiments where the electrolyte mixes with the ethanol wetted recessed features, as described in detail in the preceding section. After stepping to -0.54 V the current sharply rises to $-0.17 \mu\text{A}$ followed by a slow decent associated with Cu^{2+} depletion as deposition begins on the bottom surface and the immediately adjacent region of the sidewalls. This is followed by a current inflection near 10 min that correlates to further reduction of the growth area during the transition to purely bottom-up filling, as reflected in the growth front profiles at 6 and 12 min shown in Fig. 1b. Following the brief rise in current to a local maximum near $-0.13 \mu\text{A}$, the advancing profile permits the suppressor phase to reform and the current descends to a final passive current plateau of $\approx -0.02 \mu\text{A}$ for the workpiece. Stepping to a more aggressive applied potential of -0.56 V leads to an initial current in excess of $-0.20 \mu\text{A}$ followed by a slow current decay for the first few minutes as deposition develops along the lower sidewalls and via bottom; however, the resulting Cu^{2+} depletion followed by sidewall collision results in void formation by 9 min that halts further simulation. The relatively constant overpotential profiles for potentiostatic conditions in Fig. 1d reflect the minimal contribution ohmic losses have in determining the interfacial overpotential, η , as calculated by Eq. (12); the nearly constant overpotential for deposition at -0.54 V despite the large decrease in total current indicates the product with cell resistance is small over the full range of deposition current being generated. In the galvanostatic simulations, the applied potential (and thus overpotential) of the working electrode varies with time. For deposition at $-0.10 \mu\text{A}$ the overpotential transient exhibits a gradual increase as bottom-up deposition in the via progresses towards complete filling by 1 h. The increase in driving force is required to sustain the applied current in the face of increased suppressor flux as the unfilled via

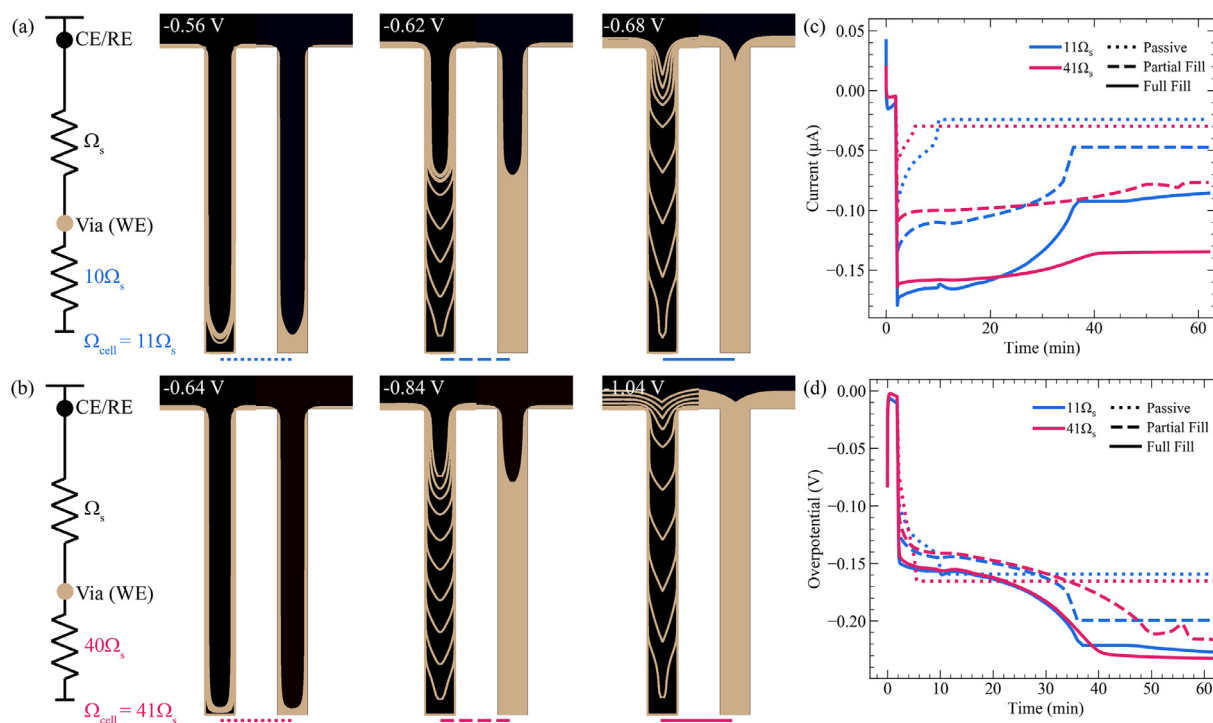


Fig. 2. Simulated growth contours in 6 min intervals (left-hand via) and final interface positions (right-hand via) for potentiostatic copper deposition in the annular via at the indicated potentials with a total uncompensated cell resistance equivalent to (a) $11\times$ and (b) $41\times$ the original cell resistance, Ω_s . Schematics show a 1-D representation of the uncompensated resistances in the circuit. Corresponding (c) current and (d) overpotential, η , transients are included for the passive (-0.56 V , -0.64 V), partial fill (-0.62 V , -0.84 V) and full fill (-0.68 V , -1.01 V) characteristic deposition profiles.

depth decreases and the corresponding gradients become steeper. A doubling of the applied current to $-0.20\ \mu\text{A}$ yields a higher overpotential close to -0.16 V that remains constant during a period of conformal growth on the lower sidewalls and bottom surface until sidewall impingement and void formation halts the simulation, analogous to the case for potentiostatic deposition at an excessively negative applied potential of -0.56 V .

Fig. 2 shows simulated final growth profiles alongside positional contours (in 6 min intervals) for potentiostatic deposition in the annular TSV depicted in Fig. 1a but with an *additional* uncompensated resistance equal to (a) $10\Omega_s$ or (b) $40\Omega_s$ (corresponding to $11\times$ and $41\times$, respectively, higher *total* cell resistance relative to the base case). For both conditions, it is evident that the increase in resistance permits more complete filling of the annular TSV at a constant applied potential during 1 h of deposition. As with galvanostatic deposition in Fig. 1, the applied potential must be chosen appropriate to the pattern density and geometry, but, significantly, appropriate engineering of the uncompensated resistance allows full bottom-up filling at a fixed applied potential, analogous to earlier TSV filling albeit at higher Cl^- concentrations [18]. At potentials that are too positive the system fails to activate and the current is distributed uniformly across the passivated surface. When the applied potentials are too negative, a seam or void is formed; simulations (not shown) reveal that applied potentials 20 mV more negative than those shown in Fig. 2 result in seams or voids. It is noteworthy that the potential window between complete interface passivation and voided via is significantly widened with the increase in uncompensated resistance: shifting from 40 mV for partial only bottom-up filling as in Fig. 1 in the base case with $1\Omega_s$ total resistance to 140 mV with $11\Omega_s$ total resistance and 420 mV with $41\Omega_s$ total resistance. Further still, one can readily envision tuning the resistance and/or applied potential such that deposition slows down to effectively passivate (or, redistribute current evenly on the interface) just below the

via outlet, a phenomenon difficult to achieve by a galvanostatic approach.

The current and overpotential transients associated with the filling simulations are shown in Fig. 2c and Fig. 2d, respectively, categorized as *passive*, *partial fill*, or *full fill* according to the final deposition profiles (left, middle, and right, respectively, of Fig. 2a and b). In each case the current spikes to the most negative value after the initial 2 min incubation period, falling gradually as the via is filled. Current reduction occurs faster at lower applied potentials and for the smaller values of uncompensated resistance. At less reducing applied potentials (*passive*, shown as dotted lines ---), the more rapid current reduction ends with universal interface passivation and sustained deposition currents near $-0.025\ \mu\text{A}$ that are distributed over the entire deposit surfaces for both values of uncompensated resistance. The small difference in the final currents at -0.56 and -0.64 V reflects more negative overpotential for the latter as per Fig. 2d; both profiles rise quickly to $\approx -0.16\text{ V}$ and -0.165 V , respectively, at which values they remain for the duration of the 1 h simulation. The transients for the intermediate applied potentials (*partial fill*, shown as dashed lines ---) exhibit a more gradual reduction in current after the initial spike (Fig. 2c), plateauing after 35 min of deposition for the $11\Omega_s$ case and 55 min for the $41\Omega_s$ case (the latter evident in plots extending to longer times). The current in the simulation with a total uncompensated cell resistance of $11\Omega_s$ decreases (in magnitude) by about $0.06\ \mu\text{A}$ while that for $41\Omega_s$ decreases by about $0.02\ \mu\text{A}$. The more stable current profile for a higher cell resistance reflects the transition in overall behavior towards galvanostatic control. Interestingly, the current transients at intermediate (---) and more negative (*full fill*, shown as solid lines -) applied potentials exhibit similar trends, the latter simply shifted to larger deposition currents. With $11\Omega_s$ of uncompensated resistance, the current plateaus at a similar time for both applied potentials. The higher current at -0.68 V yields more sustained localized deposition that results in a fully filled via.

With $41\Omega_s$ of uncompensated resistance, continued motion explicit in the last two growth contours at -0.84 V suggests that the feature might fill completely given sufficient deposition time. The simulation at -1.04 V reaches the field (i.e., $z = 0$) sooner because of the higher overall current throughout the process (albeit more material is also deposited on the field). It is notable that the overpotential profiles for both *full fill* simulations, i.e., at -0.68 V with $11\Omega_s$ and at -1.04 V with $41\Omega_s$, are nearly identical for the majority of the simulations, with similar filling contours evident until the growth front approaches the via opening. The steadily increasing overpotential as deposition approaches the opening reflects the increased driving force required to advance the growth front due to the enhanced transport of the suppressing additives and despite the increased transport of metal ion.

Simulations of the impact of uncompensated resistance on the filling of the annular TSVs were expanded to explore the full range of applied potentials between passive and voided growth profiles, also including an intermediate value for total uncompensated resistance of $21\Omega_s$. Fig. 3a shows the lowest position on the deposit interface after 1 h of deposition for the indicated values of uncompensated resistance as a function of applied potential. As in Fig. 1, potentiostatic control with $1\Omega_s$ uncompensated resistance only achieves a fill height of $33\ \mu\text{m}$ (the next -20 mV increment of applied potential resulting in void formation). Higher uncompensated resistance expands the applied potential window between fully passive and voided filling while also permitting higher filling at constant potential; with $41\Omega_s$ of total uncompensated resistance the window is seen to span -0.68 to -1.04 V (a range of 0.36 V). The impact of each -20 mV increment on fill height decreases at more negative applied potentials, particularly for the $41\Omega_s$ data. This trend reflects the balance of transport, which scales with the concentration gradients and thus increases with $1/\text{unfilled depth}$, with the potential dependent deposition kinetics that drive disruption of the suppressor layer. Fig. 3b plots the time needed to achieve 90% fill of the annular TSV as a function of the applied potential for each resistance. Counterintuitively, higher uncompensated resistance enables faster filling of the TSV, albeit at more negative applied potentials, with $50.4\ \mu\text{m}$ of filling achieved as quickly as 38 min for $41\Omega_s$, 42 min for $21\Omega_s$, and 53 min for $11\Omega_s$. The decreased fill time with increased uncompensated resistance is associated with more stable operating currents throughout filling as in Fig. 2, consistent with a trend towards galvanostatic operation.

3.2. Deposition in cylindrical TSV

The simulations of deposition in annular TSV in the preceding section offer predictions that can be validated against prior experimental work [20]. This section explores the influence of uncompensated resistance on deposition in the more generic cylindrical TSV geometry depicted in Fig. 4a. Similar to the annular TSV, simulations of potentiostatic deposition with $1\Omega_s$ uncompensated resistance (again, determined by $L = 0.25$ cm and R_c by Eq. (1)) in the $5\ \mu\text{m}$ radius and $50\ \mu\text{m}$ tall via in Fig. 4b depict a narrow operating window between passive (-0.52 V) and voided (-0.56 V) growth profiles. Achieving a fully filled cylindrical TSV again requires a potentiodynamic waveform like that detailed in previous work [20,46–48] to progressively shift the location of the sidewall passive-active transition upwards. As with the annular TSV, galvanostatic deposition enables substantial void-free bottom up via filling at 1 h of deposition, in this case at an applied current of $-0.05\ \mu\text{A}$ as shown in Fig. 4c. However, the majority of the via is filled in the first 30 min of deposition before increased additive transport passivates deposition and shifts much of the current towards deposition on the field (not shown). Of course, galvanostatic methods still require tuning of the applied current to avoid con-

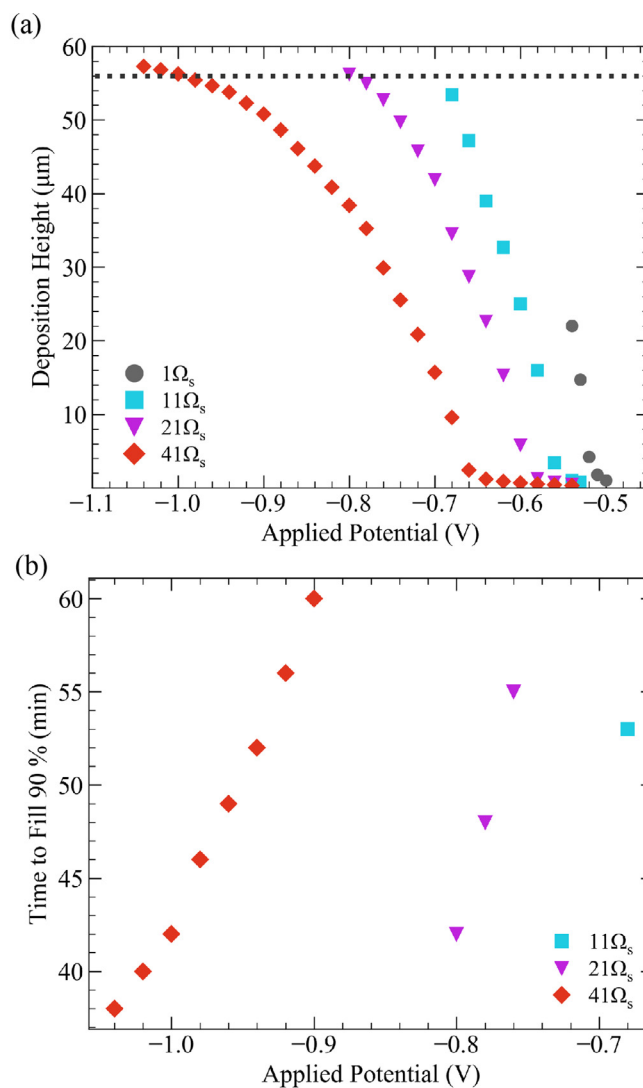


Fig. 3. (a) Chart showing the lowest position on the annular TSV interface after 1 h of deposition as a function of applied potential for the indicated total uncompensated cell resistance. Simulations 20 mV more negative of the most negative potentials shown for each resistance result in a seam or void. The dashed line represents the deposit height for a fully filled via. (b) Chart showing the time needed for the lowest position on the TSV interface to reach 90% of the via height plotted as a function of applied potential for the indicated uncompensated cell resistance. Simulations requiring more than 60 min deposition time to achieve 90% fill are not included.

formal, passive deposition on the via (as at $-0.02\ \mu\text{A}$) or voided deposits (as at $-0.08\ \mu\text{A}$). Fig. 4d and e show simulations of potentiostatic deposition with an increase in uncompensated resistance to $11\Omega_s$ and $101\Omega_s$, respectively. As with the annular geometry, simulations with the additional uncompensated resistance predict higher filling within the cylindrical TSV for the given electrolyte chemistry. After 1 h, the deposit height reaches $22\ \mu\text{m}$ (i.e., below the field) for the $10\Omega_s$ case at -0.60 V and $8\ \mu\text{m}$ for the $100\Omega_s$ case at -1.12 V. For each resistance, the simulations at potentials 20 mV more negative than these values predict a seam or void.

The behaviors uncovered thus far motivate further exploration of the effect of uncompensated resistance on the filling of even higher aspect ratio features. Fig. 5a shows simulated growth contours in 6 min intervals for the indicated control-method, operating condition, and added uncompensated resistance for the cylindrical TSV geometry presented in Fig. 4a (having an aspect ratio of 5). The condition presented (throughout Fig. 5) is the most

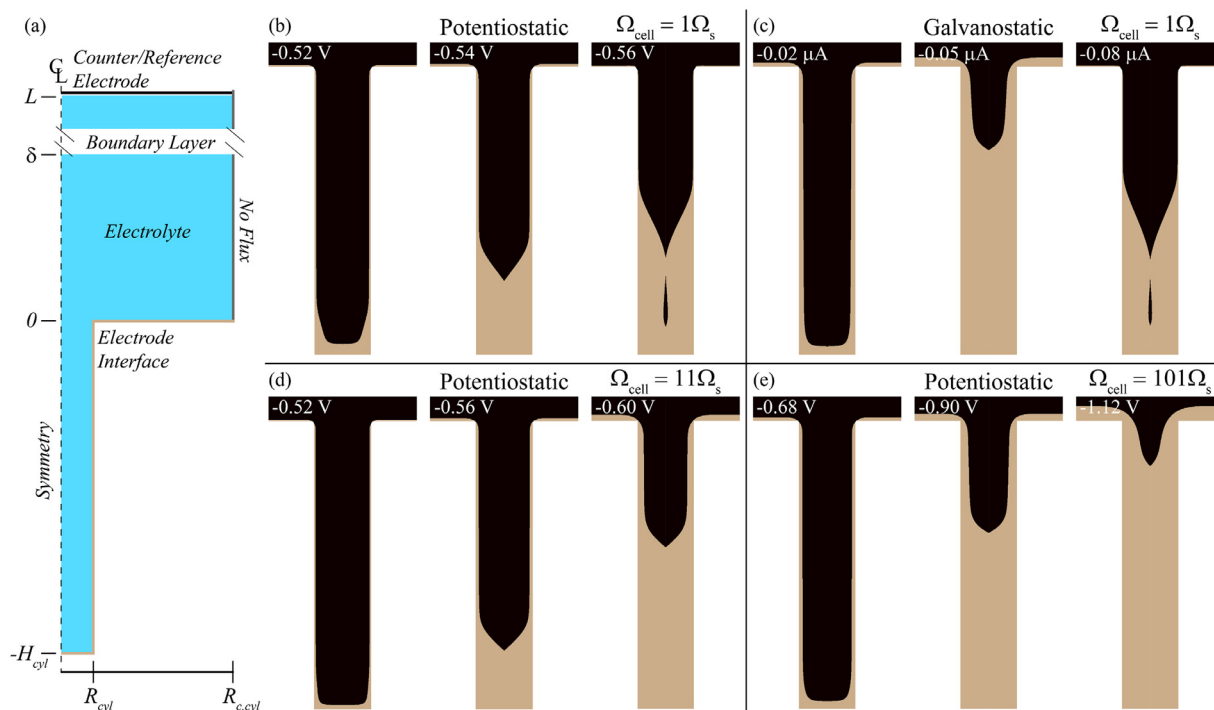


Fig. 4. (a) Schematic of the axisymmetric geometry used in the S-NDR model to simulate deposition in a cylindrical TSV with dimensions of $R_{cyl} = 5 \mu\text{m}$ and $H_{cyl} = 50 \mu\text{m}$. Relevant domains and boundaries are indicated. Simulated growth profiles for (b) potentiostatic and (c) galvanostatic copper electrodeposition after 1 h at the indicated applied potentials and currents with $1\Omega_s$ of uncompensated resistance. Simulated growth profiles after 1 h of potentiostatic copper electrodeposition with a total uncompensated cell resistance of (d) $11\Omega_s$ and (e) $101\Omega_s$.

reducing applied potential or current in 20 mV and 2 nA intervals, respectively, before simulations predict a seam. Potentiostatic deposition at -0.54 V for a cell with $1\Omega_s$ passivates shortly after 12 min of deposition, having achieved a deposit height of only 12 μm . Galvanostatic deposition at -72 nA permits active bottom-up deposition within the via for 24 min before shifting to a slower near conformal deposition mode where the last 30 min of deposition only results in the addition of 3.5 μm to the 43 μm tall deposit. This tuned current corresponds to current densities of -3.39 mA/cm^2 when scaled by projected area, -91.7 mA/cm^2 when scaled by area of the via bottom, and -1.95 mA/cm^2 when scaled by the entire electrode interface. For potentiostatic deposition with $11\Omega_s$ of uncompensated resistance an applied potential of -0.60 V yields maximum filling with active deposition for ≈ 21 min before full passivation occurs. Potentiostatic deposition with $101\Omega_s$ of total uncompensated resistance and an applied potential of -1.12 V yields maximum filling with a shift from bottom-up growth to conformal deposition after 24 min and an evolution of deposit profile that is very similar to that for galvanostatic deposition at -72 nA .

Analogous sequences of simulations are presented for cylindrical TSVs deepened to have aspect ratios of 10 and 20 ($R_{cyl} = 5 \mu\text{m}$) in Fig. 5b and 5c, respectively. In general, the trends in deposition profiles across the control-methods, with the additional uncompensated resistances increased in proportion with the via depth, match those in Fig. 5a. Specifically, potentiostatic deposition with $1\Omega_s$ results in early passivation deep within the via whereas a substantially larger uncompensated resistance shifts the final deposit height higher, with filling at the largest values approaching the height achieved using the galvanostatic approach. In higher aspect ratio vias the applied potential/current must be less reducing, regardless of control method or uncompensated resistance, to avoid Cu^{2+} depletion that induces formation of a seam or void. For galvanostatic deposition, the most reducing current is roughly

halved for each doubling of the via depth, consistent with consideration of the gradients that underlie reactant and additive transport. In terms of current densities, those in the aspect ratio 10 and 20 features correspond to -1.51 and -0.75 mA/cm^2 , respectively, when scaled by projected area, -40.7 and -20.4 mA/cm^2 , respectively, when scaled by area of the via bottom, and -0.61 and -0.19 mA/cm^2 , respectively, when scaled by the total electrode interface area. Despite use of the most aggressive applied potentials and currents compatible with void-free deposition, passivation occurs before the deposit reaches the field for each geometry. Although not the focus of this study, fill height can be increased by reducing the flux of suppressor additives either through decreased chloride concentration or reduced convective transport (i.e., increasing the boundary layer thickness in the model) with further optimization of applied potential and uncompensated resistance. The final deposit height (lowest point on the interface which, by symmetry, lies at the via middle) as functions of applied potential for the cylindrical vias with aspect ratios of 5, 10, and 20 are presented in Fig. 6a, 6b and 6c, respectively, for the indicated values of total uncompensated resistance. As with the annular geometry, the fill height for each geometry increases and the potential window between fully passive and voided filling profiles widens as the uncompensated resistance is increased.

3.3. Deposition in trench arrays

The influence of uncompensated resistance on Cu deposition in high aspect ratio features was further explored in trench arrays as depicted in the 2D geometric configuration of Fig. 7a. The trenches are 10 μm wide, 50 μm tall, 1 mm long (into the page), and are spaced 30 μm apart center-to-center ($P_t = 20 \mu\text{m}$). Simulations of galvanostatic operation produce fully filled trench arrays at currents ranging from -6 to $-30 \mu\text{A}$, the primary difference being the time necessary to achieve complete fill. Currents in excess of

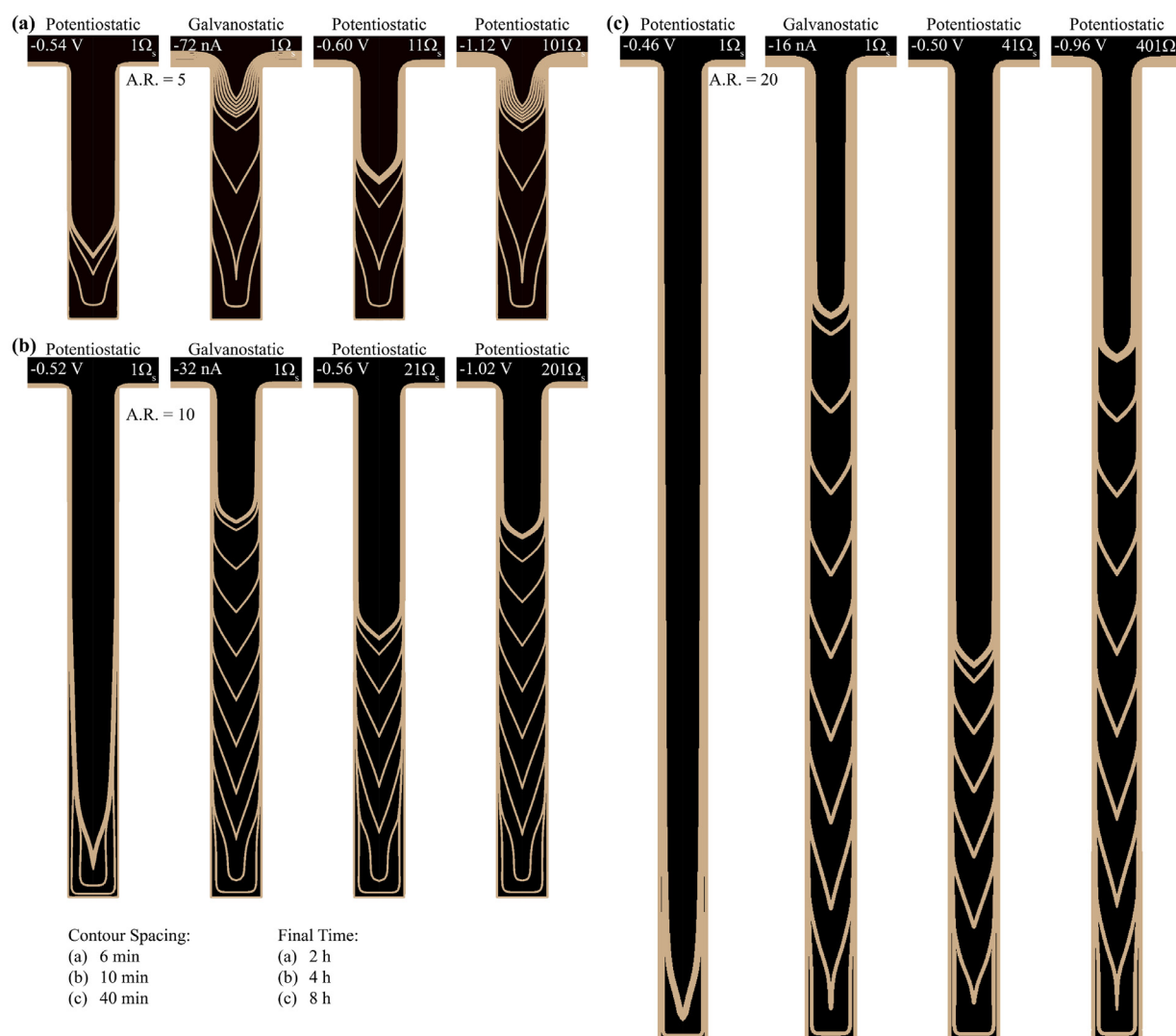


Fig. 5. Simulated growth contours for a cylindrical TSV with a 5 μm radius and heights of (a) 50 μm , (b) 100 μm , and (c) 200 μm for the indicated applied potentials/current and total uncompensated cell resistance. Final contours are at 1, 2, and 8 h with contour spacing of 6, 10, and 40 min for TSV with heights of 50 μm , 100 μm , and 200 μm , respectively. The specified applied potentials are the most negative values that do not result in seam or void formation and thus reflect the highest filling along the via centerline obtained for the given value of uncompensated resistance (in increments of 20 mV).

-30 μA produce voids towards the bottom of the trench while currents smaller than -6 μA result in conformal deposition over the entire electrode interface and, ultimately, seam or void-formation. For -30 μA of applied current, the current densities are 25 mA/cm^2 when scaling by projected area, -75 mA/cm^2 when scaling by the area of the trench bottom, and -5.77 mA/cm^2 when scaling by the entire electrode interface. Final deposit profiles and contours shown in Fig. 7b indicate the electrode interface position spaced in 10 min intervals for galvanostatic conditions that enable full filling. For all three conditions the trench array is completely filled, with deposition at -8 μA requiring 80 min longer than -30 μA . At the two higher applied currents the resulting overburden is non-uniform across the array. The interface contours (colorized to indicate time) show that deposition at -30 μA occurs uniformly in all four trenches from 2 to 32 min. After this time, deposition is localized to the 1st trench and shifts across the array from left to right. The charts in Fig. 7d show the center-line position as a function of time for each trench depicted in Fig. 7b. The profiles for all four trenches at -30 μA are identical until ≈ 32 min; shortly after this time, deposition continues in trenches 1 and 2 while trenches 3 and 4 have passivated. Eventually, trenches 3 and 4 reactivate and

achieve a similar height across the array at 52 min of deposition. At $t = 41$ min, all four trenches have reached the field (position of $y = 0$), although an ≈ 10 μm difference in fill height exists between trenches 1 and 4.

Deposition at the lower applied current of -16 μA exhibits behavior analogous to deposition at -30 μA , although deviation of height among the trenches in the array begins at a lower height within the trench after ≈ 35 min. In this case, deposition dynamically passivates and re-activates within various trenches from 35 to 95 min, at which point the profiles all merge again. Similar to the -30 μA condition, there is an ≈ 10 μm difference in deposit height between trenches 1 and 4 at $t = 67$ min; in this simulation, however, trench 1 is the last to reach the field ($y = 0$). Deviation across the trench array occurs at even earlier times for a lower applied current of -8 μA , after only 3 min of deposition and progresses in almost discrete steps, not unlike the sequential activation seen in the case of microelectrode arrays under controlled current where the total current is a globally conserved quantity [62]. At 35 min the difference in height between trenches 1 and 4 is 34 μm . After 110 min the individual trenches have all reached roughly the same height, breaking the $y = 0$ threshold at 124 min.

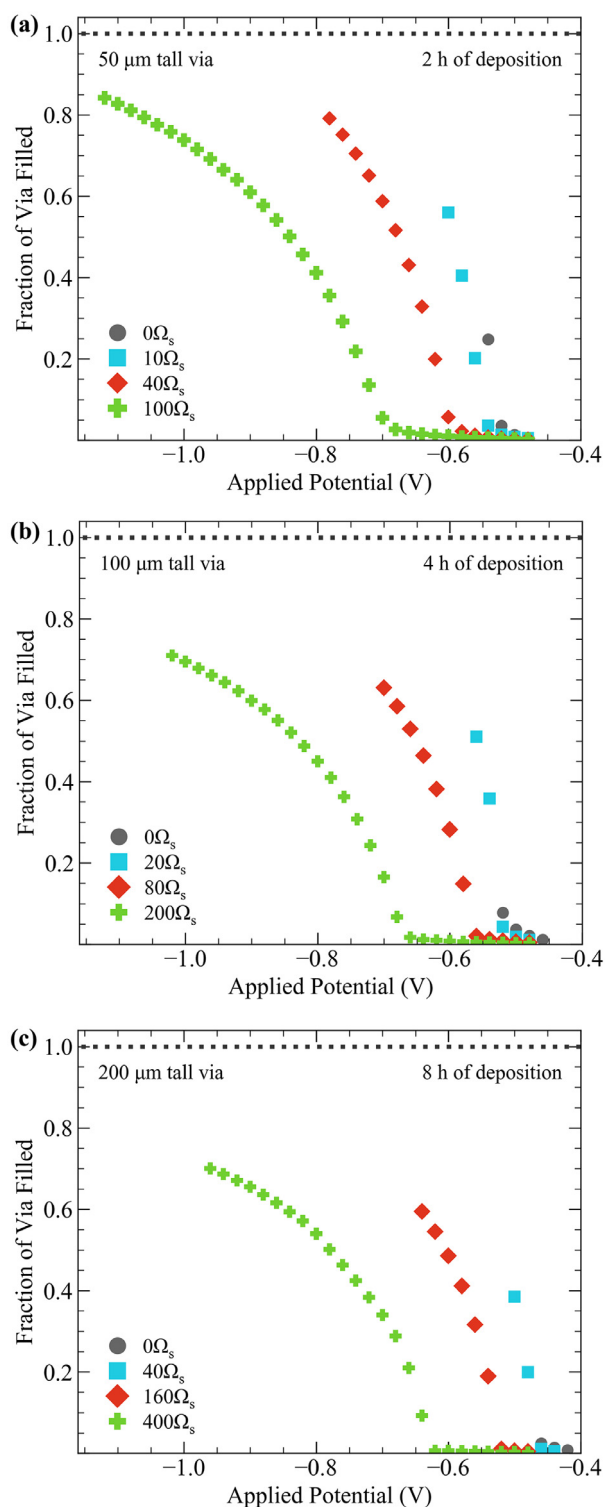


Fig. 6. Chart showing the lowest (centerline) position on the final deposit profile in the cylindrical TSV as a function of applied potential for the indicated total uncompensated cell resistances and deposition times for 5 μm radius TSV of (a) 50 μm , (b) 100 μm , and (c) 200 μm height.

Inherent to the S-NDR system is competition between interface activation driven by disruption of the suppressor layer through the metal deposition itself that is balanced against interface passivation driven by additive adsorption. In short, under galvanostatic control, higher applied currents for a given active area are associated with higher rates of deposition and increased suppressor

disruption that in the present case is associated with halide incorporation at larger overpotentials. If the applied current is sufficiently high then transport limited passivation is insufficient to shut down deposition within the feature (the transport limited suppressor flux being reduced deeper within a feature) and the deposition profiles across the array are uniform. However, the additive flux available to passivate active deposition in a feature invariably increases as filling proceeds upward. At some point, variations in the geometry between the individual features, or at least its numerical simulation, occur such that a portion of the active interface can passivate and redistribute the current to other features. Subsequently, the inverse can occur as well, where passive features reactivate and draw current from other sites. Such localized passivation and reactivation is the origin of the non-uniform profiles across the arrays in Fig. 7. Improved uniformity within the array at $-30 \mu\text{A}$ reflects the higher suppressor flux required to passivate the surface when operating at the higher deposition (and adsorbate consumption) rates, values that exceed the depth-dependent limits on additive transport down the trench throughout a greater portion of the filling process. For any value of applied current that yields localized deposition within the trenches there will necessarily be a depth at which the transport limited suppressor flux, scaling as the inverse of that depth, is sufficient to induce such instabilities. Eventually, however, the profiles all converge, indicating that the increased transport limit on suppressor flux is balanced by increased overpotential in a manner that enforces activation of all features. Both the passivation/activation of individual features and the ultimate convergence of filling contours in all features are clear for the $-8 \mu\text{A}$ profile in Fig. 7b and are also evident at longer times in the Fig. 7d charts for -16 and $-30 \mu\text{A}$.

As with the annular and cylindrical vias shown earlier, simulation of trench array filling under potentiostatic conditions in the presence of $1\Omega_s$ of uncompensated resistance has a narrow operating window between fully passive (-0.58 V) and voided deposition (-0.60 V). Deposition at -0.59 V (not shown) passivates after 30 min at a height $13 \mu\text{m}$ below the field ($y = 0$). An increase in the uncompensated resistance to $11\Omega_s$ allows for complete filling of the trench arrays in a manner similar to that seen for galvanostatic operation. The potentiostatic operating window (evaluated in 20 mV increments) is also much wider between full passivation (-0.64 V) and voided deposition (-1.02 V). Deposit profiles and interface contours for two potentiostatic conditions are shown in Fig. 7c, exhibiting evolution similar to that of the galvanostatic profiles in Fig. 7b. For the more reducing condition of -0.98 V , deposition proceeds uniformly across the array until the interface is near the field ($y = 0$) at which point individual trenches begin to oscillate between passive and active states. It takes 45 min for all trenches to reach $y = 0$ with about a $10 \mu\text{m}$ difference in height between the highest and lowest (trenches 1 and 4). In contrast, deposition at the less reducing condition of -0.72 V exhibits uniform deposition across the array until a depth of $-34 \mu\text{m}$. At this point deposition localizes into select trenches, dynamically passivating and re-activating at different heights. Deposition across the interface becomes uniform when filling in each trench approaches the field, with a height of $y = 0$ achieved for all features after 102 min.

Fig. 8 shows the global current for galvanostatic and potentiostatic conditions during deposition in the 4 trench array depicted in Fig. 7 as well as for 2 trench and 8 trench arrays under conditions that yield analogous filling. For galvanostatic operation, similar filling behavior requires scaling of the applied current with the number of features. Under potentiostatic control, the global current automatically adjusts for the increased surface area of larger arrays; the peak current at -0.98 V immediately after the pretreatment period shifts from $-14.5 \mu\text{A}$ to $-29 \mu\text{A}$ to $-58 \mu\text{A}$ as trench quantity increases from an array of 2 to 4 to 8 trenches. In fact,

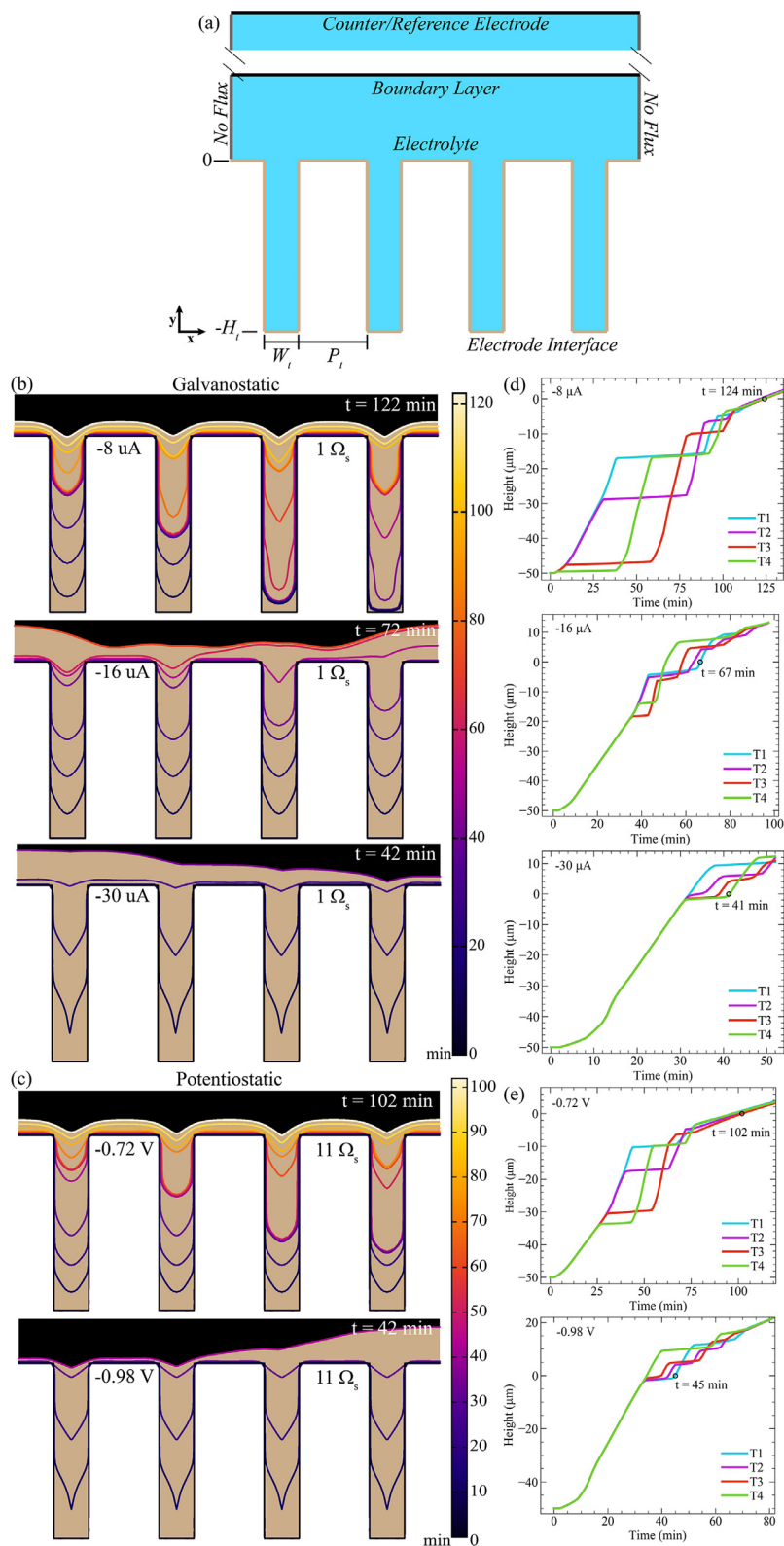


Fig. 7. (a) Schematic of the 2-D geometry used in the S-NDR model to simulate deposition in trench arrays with dimensions of $W_t = 10 \mu\text{m}$, $H_t = 50 \mu\text{m}$, $P_t = 20 \mu\text{m}$, and length of 1 mm (into the page). Simulated growth profiles for (b) galvanostatic with $1 \Omega_s$ of cell resistance and (c) potentiostatic copper electrodeposition with $11 \Omega_s$ of cell resistance at the indicated operating conditions and final times. Contour lines represent the individual trench centerline positions of the electrode interface, spaced in 10 min intervals and beginning after the pretreatment step, colored to indicate time. (d,e) Charts showing the centerline position of the growth front for each individual trench (denoted as T1, T2, T3, and T4 from left-to-right) as time progresses with annotations indicating the time when all trenches reach $y = 0$.

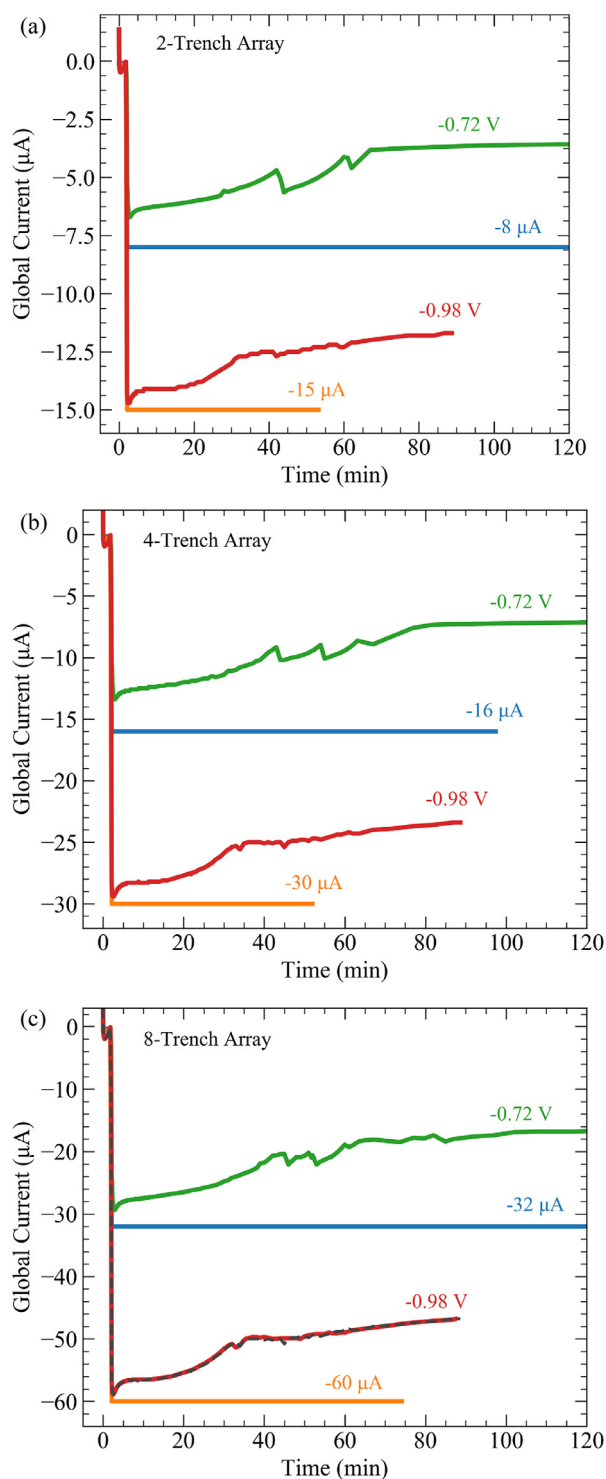


Fig. 8. Global current responses during galvanostatic and potentiostatic deposition at the indicated conditions with a total uncompensated cell resistance of $11\Omega_s$ for arrays of (a) 2 trenches, (b) 4 trenches, and (c) 8 trenches. Galvanostatic currents scale with the number of trenches as required to obtain similar (albeit not entirely identical) filling.

the current profiles at -0.98 V fall directly on top of each other when scaling for the number of trenches, as demonstrated by the dashed gray line in Fig. 8c representing the current profile at -0.98 V in a 4-trench array that has been doubled after the simulation. Thus, a potentiostatic approach may be advantageous for depositing on wafers or dies with an unknown recessed surface area,

unknown dimensions, or number of features that vary experiment-to-experiment. The noise associated with passivation of individual trenches under potential control (e.g., at -720 mV) is reduced for larger trench arrays; in a 2-trench array passivation of a single trench impacts 50% of the active surface area versus only 12.5% in an 8-trench array.

3.3.1. Deposition in trench arrays of varying width

The influence of the control mode on copper deposition behavior is further explored in trench arrays where the trenches have multiple widths as shown in Fig. 9. Trench height and edge-to-edge spacing are fixed at 50 μm and 20 μm , respectively, in a periodic array of adjacent 10 , 20 , and 30 μm wide features. In contrast to the uniform array in Figs. 7 and 8, galvanostatic simulations in an array of trenches of varying widths indicate a smaller and discontinuous operational window for void-free filling. Simulations at -5 μA produce conformal deposition on the electrode interface and, examined in 2.5 μA increments, deposition at -10 μA , -20 μA , and all currents greater than -30 μA result in void formation; examples of voided deposition are shown in Fig. 9 at -10 and -40 μA . Void formation at the lower applied currents (i.e., -10 and -20 μA) is caused by activation and localization of applied current to the narrowest trench. For applied currents greater than -30 μA , deposition occurs across the trench array but at a rate sufficient to deplete metal ion in the narrowest trench leading to void formation. Interestingly, all other conditions between -5 and -35 μA (again, in 2.5 μA intervals) produce fully filled trench arrays; examples are shown in Fig. 9 at -7.5 and -25 μA . For the less aggressive applied current value, filling of the trenches progresses individually and sequentially; deposition occurs in trench 1 (narrowest) from 2 to 25 min, trench 2 (intermediate) from 26 to 70 min, and trench 3 (widest) from 71 to 132 min. The local deposition on all three trenches slows after 155 min as the filling profile approaches the free surface with slightly varying heights across the array. Deposition at -25 μA , in contrast, occurs evenly across all three trenches until ≈ 10 min when the deposition rate accelerates in the smallest trench until it temporarily passivates at a height of -22 μm for about 20 min. This cycle of passivation and re-activation occurs once more before the deposit height reaches $y = 0$. Deposition in trench 2 behaves similarly, cycling between passive and active but lagging behind trench 1, whereas trench 3 remains active until the deposit breaches the opening and passivates at a height of 8 μm . Interestingly, the smallest trench is the last to reach a height of $y = 0$, occurring after 62 min of deposition. The overfill on the field is non-uniform, similar to that observed for galvanostatic deposition in an array of identical trenches.

Unlike galvanostatic deposition, or even potentiostatic deposition in a uniform array, simulations of potentiostatic deposition for the base case with $1\Omega_s$ results in either conformal deposition or voided filling in the varying width trench array in Fig. 9. At -0.57 V and applied potentials more positive, negligible deposition occurs and is largely conformal in nature. Deposition at applied potentials between -0.58 and -0.605 V, examined in 5 mV intervals, produces a void in the narrowest trench while the wider trench 2 and trench 3 remain passive. Simulations of deposition at -0.61 V and more negative potentials produce a fully activated trench array but with sufficient cupric ion depletion that a void forms in the narrowest trench, halting the simulations. Significantly, increasing the uncompensated resistance enables complete void-free filling of the varying width trench array. With $6\Omega_s$ of total uncompensated cell resistance, deposition at potentials of -0.60 V and more positive values results in conformal deposition. A more negative applied potential of -0.63 V yields iterative trench filling similar to that at the -7.5 μA galvanostatic condition except a transition to the passive state occurs for all 3 trenches after 100 min at heights

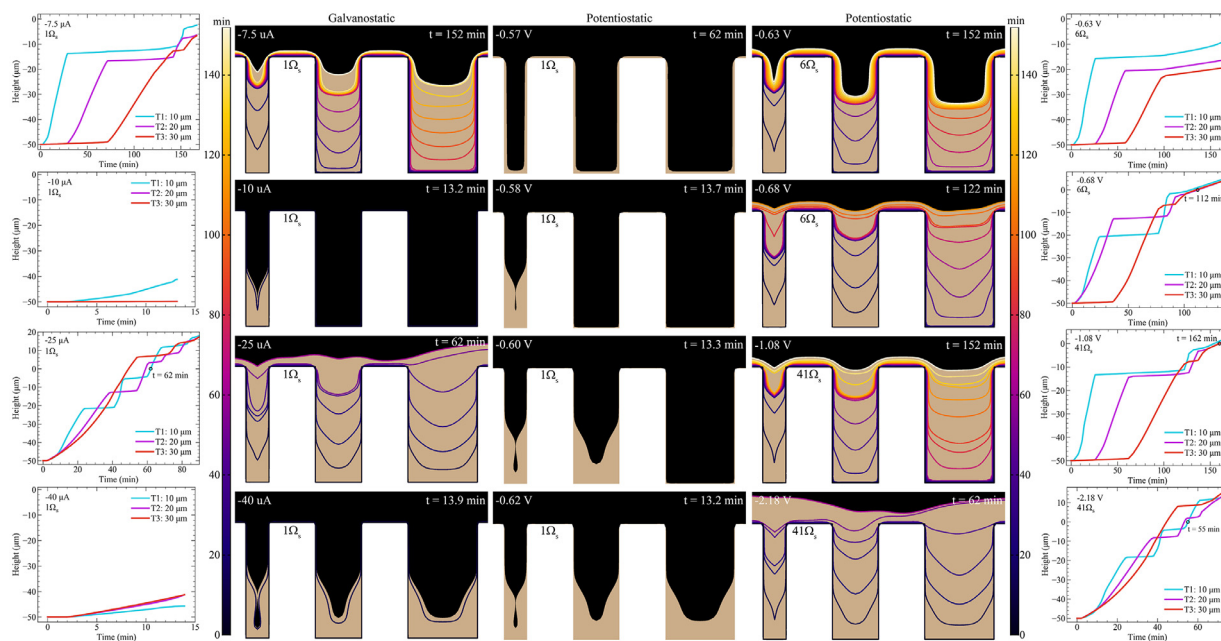


Fig. 9. Simulated growth profiles for galvanostatic and potentiostatic copper electrodeposition at the indicated operating conditions, final times, and total uncompensated cell resistances ($1\Omega_s$, $6\Omega_s$, or $41\Omega_s$) in a trench array of varying widths: 10, 20, and 30 μm from left-to-right. Contour lines represent the position of the growth front, spaced in 10 min intervals and beginning after the pretreatment step, colored to indicate time. Charts show the centerline position of the growth front of each individual trench (denoted as T1, T2, and T3 from left-to-right) as time progresses with annotations indicating the time at which all trenches reach $y = 0$.

of -15, -20, and -22 μm from left to right. For a more reducing applied potential of -0.68 V, deposition initially occurs in trenches 1 and 2 alone while trench 3 remains passive, with all three trenches eventually reaching the field ($y = 0$) after 112 min. Voiding occurs at potentials more negative than -0.82 V and at -0.64 V, the latter case is similar to the -10 μA galvanostatic condition with localization of all current to trench 1.

Increasing the uncompensated cell resistance makes potentiostatic deposition behave more like galvanostatic deposition. With a $41\Omega_s$ uncompensated resistance, the operating window between fully passive (-0.78 V) and voided fill (-2.38 V) is greatly widened. However, simulations within this range, examined in 100 mV increments, show intermediate potentials can produce voids similar to the galvanostatic conditions seen in Fig. 9; specifically at -1.18 and -1.68 V for the present geometry. Simulations at a less aggressive applied potential of -1.08 V predict individual filling similar to -0.63 V with a $6\Omega_s$ uncompensated resistance. However, interface passivation occurs higher in the trench and filling eventually reaches $y = 0$ after 162 min with only minor height variation across the array. Deposition at a more reducing applied potential of -2.18 V initially exhibits more uniform growth across the trench array, with individual trench passivation occurring sequentially in order of increasing trench width. The time at which all trenches reach a height of $y = 0$ is shortened, occurring after 55 min of deposition, but with a larger 10 μm height variation across the array. The time-dependent deposit profiles and plots of fill height for potentiostatic deposition at -2.18 V and galvanostatic deposition at -25 μA show similar characteristics for each trench width; potentiostatic control differs little from galvanostatic control, the global current at -2.18 V with the large $41\Omega_s$ uncompensated resistance showing little variation, peaking at -29.3 μA shortly after the pretreatment step and gradually decaying to -27.7 μA after 1.5 h of deposition.

3.3.2. Deposition in trench arrays of varying height

Copper deposition is explored in an even more complex trench array of varying depths in Fig. 10; trench width and edge-to-edge

spacing is 10 μm and 20 μm , respectively, in a periodic array of adjacent 50, 75, and 100 μm deep features. Simulations of galvanostatic deposition predict fully filled trench arrays at conditions between -4 and -8 μA . Deposition at an applied current less than -4 μA results in conformal deposition or bottom-up fill that does not achieve fully filled heights of $y = 0$ after 5 h while conditions more aggressive than -8 μA produce a void in the deepest trench. Simulations of deposition at -4.5 μA show preferential filling of the deepest trench for the first 90 min before passivation occurs with a shift to deposition in the middle trench. After an additional 50 min a similar transition occurs with deposition shifting to the shallowest trench. After 220 min all three trenches are at approximately the same height, although still lower than the field at $y = 0$. The filling profile is similar at -7.5 μA , except the applied current is sufficient to activate the middle trench immediately after the pretreatment step. Deposition in trenches 2 and 3 is sustained for 45 min and 75 min, respectively, before passivation. The shallowest trench remains passive for the first 80 min before significant filling occurs. As the deposit nears the trench outlets the differences in height lessen across the array. By 145 min there is minimal variation in trench height and all features have reached the position of the field ($y = 0$). As expected, deposition at the more aggressive current of -7.5 μA achieves complete filling ≈ 100 min faster than -4.5 μA .

Similar to deposition in the other trench arrays (Figs. 7 and 9), potentiostatic deposition with only $1\Omega_s$ in uncompensated resistance cannot achieve complete filling of the array prior to passivation. The fill height of the trenches in the array at the most negative applied potential before voiding occurs are only -49, -57, and -53 μm from shortest to tallest (not shown). The smallest value of uncompensated resistance predicted to enable a fully filled profile at a single applied potential is $9\Omega_s$ (evaluated in $1\Omega_s$ intervals) where complete filling occurs within 4 h at -0.66 V as shown in Fig. 10. Filling under these conditions has similarities to galvanostatic deposition at -7.5 μA ; namely, deposition is initially localized to trenches 2 and 3 while trench 1 remains passive for the first 75 min. A significant portion of the feature filling time is

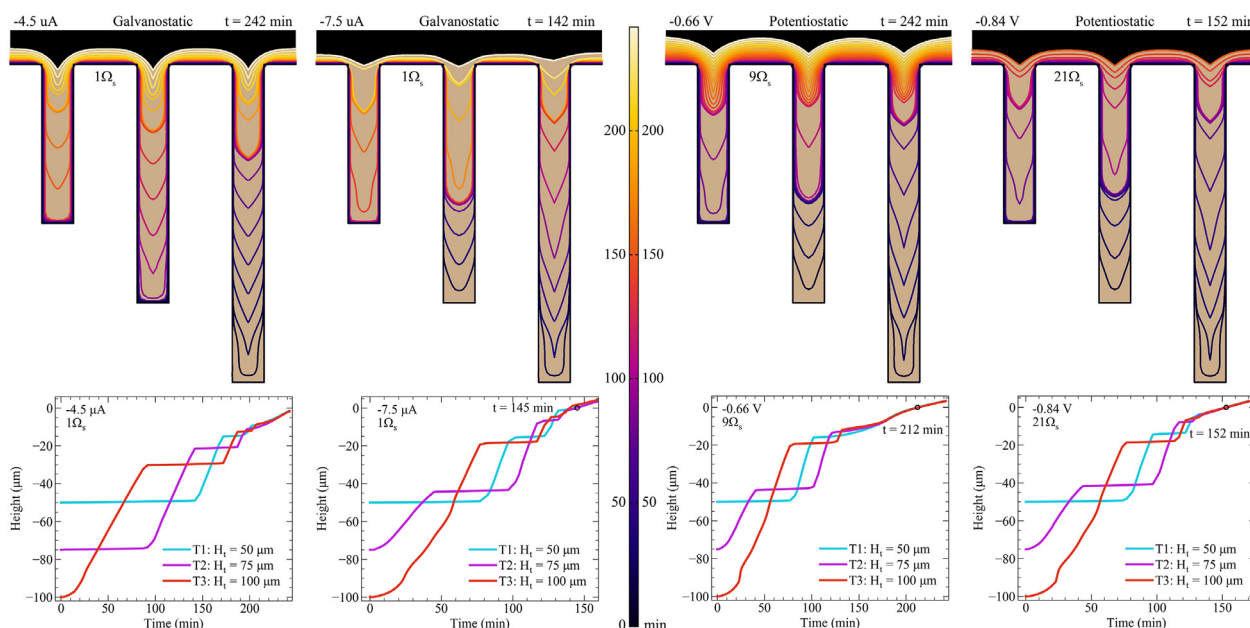


Fig. 10. Simulated growth profiles for galvanostatic and potentiostatic copper electrodeposition at the indicated operating conditions, uncompensated cell resistance ($1\Omega_s$, $9\Omega_s$, or $21\Omega_s$), and final times in a trench array of varying heights: 50 , 75 , and 100 μm from left-to-right. Contour lines represent the position of the growth front, spaced in 10 min intervals and beginning after the pretreatment step, colorized to indicate time. Charts show the centerline position of the growth front for each individual trench (denoted as T1, T2, and T3 from left-to-right) as time progresses with annotations indicating the time at which all trenches reach $y = 0$.

associated with slower conformal deposition that occurs after ≈ 130 min, apparent in the closely spaced contours and thick deposit on the field. The centerline of the trenches only reaches the field ($y = 0$) after 212 min. Increasing the total uncompensated cell resistance to $21\Omega_s$ permits faster filling of the trench array through potentiostatic operation at the more negative -0.84 V. Analogous to the $9\Omega_s$ simulation, the shallowest trench remains passive for the first 75 min while deposition proceeds in the other two trenches. Finally, a shift to conformal deposition across the workpiece occurs after ≈ 130 min with a smaller height variation across the interface compared to that seen for the $9\Omega_s$ simulation. The smaller remaining height for the final stage of conformal deposition enables the $21\Omega_s$ simulation to achieve the $y = 0$ threshold after only an additional 22 min ($t = 152$ min) of deposition. Seam or void-formation is predicted at potentials 20 mV more negative than the two potentiostatic conditions in Fig. 10.

4. Conclusions

Bottom-up via and trench filling has been demonstrated for a variety of additive-derived S-NDR metal deposition systems. The simulations in the present work indicate that with appropriate optimization of the applied current, galvanostatic Cu deposition from a polyether – Cl^- suppressed $\text{CuSO}_4 - \text{H}_2\text{SO}_4$ electrolyte can completely fill high-aspect ratio via and trench features for dimensions congruent with previous experimental work [45,49]. While the same is true for potentiostatic conditions, deposition under conditions where the uncompensated resistance is minimized often results in passivation before feature filling is complete. Potentiodynamic waveforms have been previously explored to overcome this limitation [20,46–48]. This work explores the utility of manipulating instead the uncompensated resistance of the electrochemical cell to help modulate and improve potentiostatic controlled feature filling. This may be implemented in a number of ways, from judicious positioning of the reference electrode, to insertion of a baffle that increases the effective resistivity of the electrolyte, to the addition of an external series resistor. The last is

arguably the simplest to implement as a resistive contact to the working electrode in a 3-electrode system and, more generally, a series resistor located anywhere in a 2-electrode circuit. The current response during potentiostatic deposition in S-NDR systems with a significant uncompensated resistance begins to approach that seen for galvanostatic control. This not only helps establish conditions where complete feature filling is possible but also significantly broadens the processing window making the method more robust to variations in the workpiece geometry, from trench dimensions to patterning effects. Particularly interesting characteristics are captured for feature arrays of both uniform and variable dimensions where sequential filling of different sized features is predicted as well as oscillation between passivation and reactivation during filling under different conditions. Even more complex behavior can occur with discontinuities appearing in the processing window where periodic transitions between complete filling and void formation occur as the control parameter (potential or current) is changed monotonically. All of the above reflect the strong path-dependent behavior that arises in non-linear bifurcation reactions, especially those where a rapid electrical response is globally coupled to slower, locally non-uniform and mass transport constrained, mixed control reactions as evidenced in additive induced S-NDR systems.

Declaration of Competing Interest

The authors declare that they have no known competing financial interests or personal relationships that could have appeared to influence the work reported in this paper.

Credit authorship contribution statement

T.M. Braun: Conceptualization, Methodology, Formal analysis, Visualization, Writing - original draft. **D. Josell:** Conceptualization, Writing - review & editing. **T.P. Moffat:** Conceptualization, Supervision, Writing - review & editing.

Acknowledgments

Identification of commercial products in this paper is done to specify the experimental procedure. In no case does this imply endorsement or recommendation by the National Institute of Standards and Technology (NIST).

References

- [1] T.P. Moffat, J.E. Bonevich, W.H. Huber, A. Stanishevsky, D.R. Kelly, G.R. Stafford, D. Josell, Superconformal electrodeposition of copper in 500-90nm features, *J. Electrochem. Soc.* 147 (2000) 4524.
- [2] T.P. Moffat, D. Wheeler, D. Josell, Electrodeposition of copper in the SPS-PEG-Cl additive system – I. kinetic measurements: influence of SPS, *J. Electrochem. Soc.* 151 (2004) C262.
- [3] T.P. Moffat, D. Wheeler, M.D. Edelstein, D. Josell, Superconformal film growth: mechanism and quantification, *IBM J. Res. Dev.* 49 (2005) 19.
- [4] S.K. Kim, D. Josell, T.P. Moffat, Electrodeposition of Cu in the PEI-PEG-Cl-SPS additive system: reduction of overflow bump formation during superfilling, *J. Electrochem. Soc.* 153 (2006) C616.
- [5] S.K. Kim, D. Josell, T.P. Moffat, Cationic surfactants for the control of overflow bumps in Cu superfilling, *J. Electrochem. Soc.* 153 (2006) C826.
- [6] M.A. Pasquale, L.M. Gassa, A.J. Arvia, Copper electrodeposition from an acidic plating bath containing accelerating and inhibiting organic additives, *Electrochim. Acta* 53 (2008) 5891.
- [7] M. Tan, C. Guymon, D. Wheeler, J.N. Harb, The role of SPS, MPSA, and chloride in additive systems for copper electrodeposition, *J. Electrochem. Soc.* 154 (2007) D78.
- [8] P. Broekmann, A. Fluegel, C. Emnet, M. Arnold, C. Roeger-Goepfert, A. Wagner, H.T.M. Nguyen, D. Mayer, Classification of suppressor additives based on synergistic and antagonistic ensemble effects, *Electrochim. Acta* 56 (2011) 4724.
- [9] P.M. Vereecken, R.A. Binstead, H. Delgianni, P.C. Andricacos, The chemistry of additives in damascene copper plating, *IBM J. Res. Dev.* 49 (2005) 3.
- [10] M. Tan, J.N. Harb, Additive behavior during copper electrodeposition in solutions containing Cl⁻, PEG, and SPS, *J. Electrochem. Soc.* 150 (2003) C420.
- [11] C.H. Chen, C.W. Lu, S.M. Huang, W.P. Dow, Effects of supporting electrolytes on copper electroplating for filling through-hole, *Electrochim. Acta* 56 (2011) 5954.
- [12] W.P. Dow, H.S. Huang, Z. Lin, Interactions between brightener and chloride ions on copper electroplating for laser-drilled via-hole filling, *Electrochem. Solid St.* 6 (2003) C134.
- [13] T.M. Braun, S.H. Kim, H.J. Lee, T.P. Moffat, D. Josell, Superconformal nickel deposition in through silicon vias: experiment and prediction, *J. Electrochem. Soc.* 165 (2018) D291.
- [14] D. Josell, T.P. Moffat, Superconformal bottom-up nickel deposition in high aspect ratio through silicon vias, *J. Electrochem. Soc.* 163 (2016) D322.
- [15] D. Josell, M. Silva, T.P. Moffat, Superconformal bottom-up cobalt deposition in high aspect ratio through silicon vias, *J. Electrochem. Soc.* 163 (2016) D809.
- [16] D. Josell, T.P. Moffat, Superconformal bottom-up gold deposition in high aspect ratio through silicon vias, *J. Electrochem. Soc.* 164 (2017) D327.
- [17] D. Josell, T.P. Moffat, Extreme bottom-up filling of through silicon vias and damascene trenches with gold in a sulfite electrolyte, *J. Electrochem. Soc.* 160 (2013) D3035.
- [18] T.P. Moffat, D. Josell, Extreme bottom-up superfilling of through-silicon-vias by damascene processing: suppressor disruption, positive feedback and Turing patterns, *J. Electrochem. Soc.* 159 (2012) D208.
- [19] D. Josell, T.P. Moffat, Superconformal copper deposition in through silicon vias by suppression-breakdown, *J. Electrochem. Soc.* 165 (2018) D23.
- [20] T.M. Braun, D. Josell, M. Silva, J. Kildon, T.P. Moffat, Effect of chloride concentration on copper deposition in through silicon vias, *J. Electrochem. Soc.* 166 (2019) D3259.
- [21] W.P. Dow, H.H. Chen, M.Y. Yen, W.H. Chen, K.H. Hsu, P.Y. Chuang, H. Ishizuka, N. Sakagawa, R. Kimizuka, Through-hole filling by copper electroplating, *J. Electrochem. Soc.* 155 (2008) D750.
- [22] W.P. Dow, D.H. Liu, C.W. Ku, C.H. Chen, J.J. Yan, S.M. Huang, Through-hole filling by copper electroplating using a single organic additive, *Electrochem. Solid State Lett.* 14 (2011) D13.
- [23] G.Y. Lin, J.J. Yan, M.Y. Yen, W.P. Dow, S.M. Huang, Characterization of through-hole filling by copper electroplating using a tetrazolium salt inhibitor, *J. Electrochem. Soc.* 160 (2013) D3028.
- [24] P. Ogutu, E. Fey, N. Dimitrov, Superconformal filling of high aspect ratio through glass vias (TGV) for interposer applications using TNBT and NTBC additives, *J. Electrochem. Soc.* 162 (2015) D457.
- [25] L. Yang, A. Radisic, J. Deconinck, P.M. Vereecken, Stochastic modeling of polyethylene glycol as a suppressor in copper electroplating, *J. Electrochem. Soc.* 161 (2014) D269.
- [26] G.-K. Liu, S. Zou, D. Josell, L.J. Richter, T.P. Moffat, SEIRAS study of chloride-mediated polyether adsorption on Cu, *J. Phys. Chem. C* 122 (2018) 21933.
- [27] M.R. Hill, G.T. Rogers, Polyethylene-glycol in copper electrodeposition onto a rotating-disk electrode, *J. Electroanal. Chem.* 86 (1978) 179.
- [28] M. Yokoi, S. Konishi, T. Hayashi, Adsorption behavior of polyoxyethyleneglycole on the copper surface in an acid copper-sulfate bath, *Denki Kagaku Oyobi Kogyo Butsuri Kagaku* 52 (1984) 218.
- [29] Z.V. Feng, X. Li, A.A. Gewirth, Inhibition due to the interaction of polyethylene glycol, chloride, and copper in plating baths: a surface-enhanced Raman study, *J. Phys. Chem. B* 107 (2003) 9415.
- [30] M. Hayase, M. Taketani, T. Hatsuzawa, K. Hayabusa, Preferential copper electrodeposition at submicrometer trenches by consumption of halide ion, *Electrochem. Solid State Lett.* 6 (2003) C92.
- [31] M. Yokoi, S. Konishi, T. Hayashi, Mechanism of the electrodeposition and dissolution of copper in an acid copper-sulfate bath .5. acceleration mechanism in the presence of Cl⁻ ions, *Denki Kagaku* 51 (1983) 460.
- [32] J.P. Healy, D. Pletcher, M. Goodenough, The chemistry of the additives in an acid copper electroplating bath .1. polyethylene-glycol and chloride-ion, *J. Electroanal. Chem.* 338 (1992) 155.
- [33] J.J. Kelly, A.C. West, Copper deposition in the presence of polyethylene glycol – I. quartz crystal microbalance study, *J. Electrochem. Soc.* 145 (1998) 3472.
- [34] K. Doblhofer, S. Wasle, D.M. Soares, K.G. Weil, G. Ertl, An EQCM study of the electrochemical copper-(II)/copper(I) system in the presence of PEG and chloride ions, *J. Electrochem. Soc.* 150 (2003) C657.
- [35] K.R. Hebert, Role of chloride ions in suppression of copper electrodeposition by polyethylene glycol, *J. Electrochem. Soc.* 152 (2005) C283.
- [36] K.R. Hebert, S. Adhikari, J.E. Houser, Chemical mechanism of suppression of copper electrodeposition by poly (ethylene glycol), *J. Electrochem. Soc.* 152 (2005) C324.
- [37] M.L. Walker, L.J. Richter, T.P. Moffat, *In situ* ellipsometric study of PEG/Cl⁻ co-adsorption on Cu, Ag, and Au, *J. Electrochem. Soc.* 152 (2005) C403.
- [38] W.P. Dow, M.Y. Yen, W.B. Lin, S.W. Ho, Influence of molecular weight of polyethylene glycol on microvia filling by copper electroplating, *J. Electrochem. Soc.* 152 (2005) C769.
- [39] M.J. Willey, A.C. West, Microfluidic studies of adsorption and desorption of polyethylene glycol during copper electrodeposition, *J. Electrochem. Soc.* 153 (2006) C728.
- [40] M.J. Willey, E.J. McNerney, Adsorption and desorption kinetics of block copolymer wetting agent used in copper electroplating, *J. Electrochem. Soc.* 156 (2009) D98.
- [41] M.E. Huerta-Garrido, M.D. Pritzker, Inhibition of copper deposition by polyethylene glycol and chloride II. Analysis and application, *J. Electrochem. Soc.* 156 (2009) D175.
- [42] M.E. Huerta-Garrido, M.D. Pritzker, Inhibition of copper deposition by polyethylene glycol and chloride I. Model development and parameter estimation, *J. Electrochem. Soc.* 156 (2009) D36.
- [43] D. Josell, D. Wheeler, T.P. Moffat, Modeling extreme bottom-up filling of through silicon vias, *J. Electrochem. Soc.* 159 (2012) D570.
- [44] D. Wheeler, T.P. Moffat, D. Josell, Spatial-temporal modeling of extreme bottom-up filling of through-silicon-vias, *J. Electrochem. Soc.* 160 (2013) D3260.
- [45] L. Yang, A. Radisic, J. Deconinck, P.M. Vereecken, Modeling the bottom-up filling of through-silicon vias through suppressor adsorption/desorption mechanism, *J. Electrochem. Soc.* 160 (2013) D3051.
- [46] L.A. Menk, D. Josell, T.P. Moffat, E. Baca, M.G. Blain, A. Smith, J. Dominguez, J. McClain, P.D. Yeh, A.E. Hollowell, Bottom-up copper filling of large scale through silicon vias for MEMS technology, *J. Electrochem. Soc.* 166 (2018) D3066.
- [47] D. Josell, L.A. Menk, A.E. Hollowell, M. Blain, T.P. Moffat, Bottom-up copper filling of millimeter size through silicon vias, *J. Electrochem. Soc.* 166 (2019) D3254.
- [48] T.M. Braun, D. Josell, J. John, S. Deshpande, T.P. Moffat, Simulation of copper electrodeposition in millimeter size through-silicon vias, *J. Electrochem. Soc.* 167 (2020) 162508.
- [49] L.A. Menk, E. Baca, M.G. Blain, J. McClain, J. Dominguez, A. Smith, A.E. Hollowell, Galvanostatic plating with a single additive electrolyte for bottom-up filling of copper in mesoscale TSVs, *J. Electrochem. Soc.* 166 (2019) D3226.
- [50] I. Krastev, M.T. Koper, Pattern-formation during the electrodeposition of a silver antimony alloy, *Physica A* 213 (1995) 199.
- [51] J. Jorne, M.G. Lee, Striated morphology during electrodeposition, *J. Electrochem. Soc.* 143 (1996) 865.
- [52] T.M. Braun, D. Josell, T.P. Moffat, Microelectrode studies of S-NDR copper electrodeposition: potentiodynamic and galvanodynamic measurements and simulations, *J. Electrochem. Soc.* 167 (2020) 082509.
- [53] N. Mazouz, K. Krischer, A theoretical study on Turing patterns in electrochemical systems, *J. Phys. Chem. B* 104 (2000) 6081.
- [54] K. Krischer, N. Mazouz, G. Flatgen, Pattern formation in globally coupled electrochemical systems with an S-shaped current-potential curve, *J. Phys. Chem. B* 104 (2000) 7545.
- [55] Y.J. Li, J. Oslonovitch, N. Mazouz, F. Plenge, K. Krischer, G. Ertl, Turing-type patterns on electrode surfaces, *Science* 291 (2001) 2395.
- [56] K. Krischer, New directions and challenges in electrochemistry – spontaneous formation of spatiotemporal patterns at the electrode vertical bar electrolyte interface, *J. Electroanal. Chem.* 501 (2001) 1.
- [57] K. Krischer, R.C. Alkire, D.M. Kolb, Nonlinear dynamics in electrochemical systems, *Advances in Electrochemical Science and Engineering*, 8, Wiley-VCH, 2002.
- [58] M.T. Koper, Non-linear phenomena in electrochemical systems, *J. Chem. Soc. Faraday Trans* 94 (1998) 1369.
- [59] N. Mazouz, G. Flatgen, K. Krischer, I.G. Kevrekidis, The impact of the operation mode on pattern formation in electrode reactions – from potentiostatic to galvanostatic control, *J. Electrochem. Soc.* 145 (1998) 2402.

- [60] R. Fang, K. Namiki, P. Vereecken, K.T. Kwietniak, B.C. Baker, K. Ide, H. Suzuki, H. Kanda, K. Mishima, K. Musaka, L. Delgianni, ULSI and MEMS ECS PV, in: Proceedings of the Uniform Copper Electroplating on Resistive Substrates, 2005, p. 193.
- [61] D. A., A. Bonnefont Crespo-Yapur, R. Schuster, K. Krischer, E.R. Savinova, Co-operative behaviour of Pt microelectrodes during CO bulk electrooxidation, *ChemPhysChem* 14 (2013) 1117.
- [62] S. Bozdech, Y. Biecher, E.R. Savinova, R. Schuster, K. Krischer, A. Bonnefont, Oscillations in an array of bistable microelectrodes coupled through a globally conserved quantity, *Chaos* 28 (2018) 045113.
- [63] T.I. Quickenden, Q.Z. Xu, Toward a reliable value for the diffusion coefficient of cupric ion in aqueous solution, *J. Electrochem. Soc.* 143 (1996) 1248.
- [64] J.S. Newman, *Electrochemical Systems*, Wiley, Hoboken, NJ, 2004.
- [65] R.A. Waggoner, F.D. Blu, J.C. Lang, Diffusion in aqueous-solutions of poly(ethylene glycol) at low concentrations, *Macromolecules* 28 (1995) 2658.
- [66] L. Masaro, X.X. Zhu, P.M. Macdonald, Self-diffusion of oligo- and poly(ethylene glycol)s in poly(vinyl alcohol) aqueous solutions as studied by pulsed-gradient NMR spectroscopy, *Macromolecules* 31 (1998) 3880.
- [67] K. Shimada, H. Kato, T. Saito, S. Matsuyama, S. Kinugasa, Precise measurement of the self-diffusion coefficient of poly(ethylene glycol) in aqueous solution using uniform oligomers, *J. Chem. Phys.* 122 (2005).
- [68] J. Gonzalez-Lopez, C. Alvarez-Lorenzo, P. Taboada, A. Sosnik, I. Sandez-Macho, A. Concheiro, Self-associative behavior and drug-solubilizing ability of poloxamine (Tetronic) block copolymers, *Langmuir* 24 (2008) 10688.
- [69] J.F. Dong, J. Armstrong, B.Z. Chowdhry, S.A. Leharne, Thermodynamic modelling of the effect of pH upon aggregation transitions in aqueous solutions of the poloxamine, T701, *Thermochim. Acta* 417 (2004) 201.